

In-sector Compressive Beam Acquisition for MmWave and THz Radios

Masoumi, Hamed; Verhaegen, Michel; Myers, Nitin Jonathan

DOI

[10.1109/TCOMM.2024.3472532](https://doi.org/10.1109/TCOMM.2024.3472532)

Publication date

2024

Document Version

Final published version

Published in

IEEE Transactions on Communications

Citation (APA)

Masoumi, H., Verhaegen, M., & Myers, N. J. (2024). In-sector Compressive Beam Acquisition for MmWave and THz Radios. *IEEE Transactions on Communications*, 73(4), 2752-2768. <https://doi.org/10.1109/TCOMM.2024.3472532>

Important note

To cite this publication, please use the final published version (if applicable). Please check the document version above.

Copyright

Other than for strictly personal use, it is not permitted to download, forward or distribute the text or part of it, without the consent of the author(s) and/or copyright holder(s), unless the work is under an open content license such as Creative Commons.

Takedown policy

Please contact us and provide details if you believe this document breaches copyrights. We will remove access to the work immediately and investigate your claim.

Green Open Access added to TU Delft Institutional Repository

'You share, we take care!' - Taverne project

<https://www.openaccess.nl/en/you-share-we-take-care>

Otherwise as indicated in the copyright section: the publisher is the copyright holder of this work and the author uses the Dutch legislation to make this work public.

In-Sector Compressive Beam Acquisition for mmWave and THz Radios

Hamed Masoumi¹, *Graduate Student Member, IEEE*, Michel Verhaegen², *Member, IEEE*,
and Nitin Jonathan Myers³, *Member, IEEE*

Abstract—Beam acquisition is key in enabling millimeter wave and terahertz radios to achieve their capacity. Due to the use of large antenna arrays in these systems, the common exhaustive beam scanning results in a substantial training overhead. Prior work has addressed this issue by developing compressive sensing (CS)-based methods which exploit channel sparsity for faster beam acquisition. Unfortunately, most CS techniques employ wide beams and suffer from a low signal-to-noise ratio (SNR) in the channel measurements. To solve this challenge, we develop an IEEE 802.11ad/ay compatible technique that takes an in-sector approach for CS. In our method, the angle domain channel is partitioned into several sectors, and the channel within the best sector is estimated and then used for beamforming. The essence of our framework lies in the construction of a low-resolution beam codebook to identify the best sector and in the design of a CS matrix optimized for in-sector channel estimation. Our beam codebook illuminates distinct non-overlapping sectors and can be realized with low-resolution phased arrays. We show that the proposed codebook results in a higher received SNR than the state-of-the-art sector sweep codebooks. Furthermore, our optimized CS matrix achieves a better in-sector channel reconstruction and a higher achievable rate than comparable benchmarks.

Index Terms—Compressed sensing, mm-Wave, THz, beamforming, phased array, sector sweep.

I. INTRODUCTION

MILLIMETER wave (mmWave) and terahertz (THz) radios will be an integral part of 6G, as they exploit wide bandwidths and achieve high beamforming gain with large antenna arrays [3], [4]. Finding the optimal beam at the radios through classical channel estimation or beam scanning is challenging in these systems due to the use of large arrays and hardware constraints. For instance, mmWave radios usually employ phased arrays equipped with a single radio-frequency (RF) chain to achieve a cost-effective and power-efficient architecture [5], [6]. These arrays acquire fewer spatial channel measurements than fully

digital arrays, thereby restricting the application of conventional multiple-input multiple-output channel estimation methods. Furthermore, the acquired measurements are projections of the channel on antenna weight matrices whose entries are constrained to a small alphabet. The size of this alphabet is limited due to the finite resolution of the phase shifters.

An alternative to beam scanning is hierarchical beam search, wherein beams with decreasing beamwidths are sequentially applied. At the end of the search process, a narrow beam that results in the highest received SNR is used for communication [6]. To implement hierarchical search, the design objective is to construct hardware-compatible beams that focus the transmitter's energy on a section of the channel in the angle domain. The sections are referred to as *sectors*, where each sector represents a group of directions in the angle domain. The angle domain is also commonly called the beamspace [7]. The process of identifying the best sector is called sector level sweep (SLS). Prior work has designed codebooks for SLS with high-resolution phased arrays [6], [8], [9] and low-resolution phased arrays [10], [11]. The techniques in [6], [8], [9], [10], and [11] construct contiguous sectors, i.e., sectors that cover a contiguous band of directions such as the ones shown in Fig. 3(a). In this paper, we explain that realizing such contiguous sectors with extremely low-resolution phased arrays is challenging. For example, the constructed antenna weights in [10] result in significant power leakage outside the sectors with one-bit phased arrays. To address the leakage issue, we propose new comb-like sectors that can be realized even with one-bit phased arrays.

In IEEE 802.11ad/ay devices, the transmitter discerns the *sector of interest* by finding the sector that results in the highest received power. Then, the beam refinement protocol (BRP) can be used to obtain channel measurements and subsequently perform beamforming within the sector of interest. Unfortunately, exhaustive beam scanning within this sector can still result in a huge overhead in mmWave or THz radios with massive antenna arrays. To address this problem, prior work has exploited the sparse or low-rank characteristics of the angle domain channel [12], [13] for sub-Nyquist channel estimation. Most of these techniques [14], [15], [16], [17], however, employ quasi-omnidirectional beams to acquire spatial channel measurements. The use of such wide beams results in a poor signal-to-noise ratio (SNR) in the channel measurements, causing these methods to fail in practice [11]. Therefore, a collection of beams that focus energy only within

Received 25 January 2024; revised 3 July 2024 and 21 September 2024; accepted 24 September 2024. Date of publication 2 October 2024; date of current version 18 April 2025. An earlier version of this paper was presented in part at Proceedings of the IEEE Signal Processing Advances in Wireless Communications (SPAWC) in 2022 [DOI: 10.1109/SPAWC51304.2022.9833949] and in part at the 2023 IEEE Statistical Signal Processing (SSP) Workshop [2]. The associate editor coordinating the review of this article and approving it for publication was G. A. Aruma Baduge. (*Corresponding author: Nitin Jonathan Myers.*)

The authors are with Delft Center for Systems and Control, Delft University of Technology, 2628 CD Delft, The Netherlands (e-mail: h.masoumi@tudelft.nl; m.verhaegen@tudelft.nl; n.j.myers@tudelft.nl).

Digital Object Identifier 10.1109/TCOMM.2024.3472532

0090-6778 © 2024 IEEE. Personal use is permitted, but republication/redistribution requires IEEE permission.
See <https://www.ieee.org/publications/rights/index.html> for more information.

the sector of interest must be developed for “in-sector” channel estimation using BRP.

We now discuss prior work on sparsity-aware channel estimation within a sector [11], [18], [19], [20], [21]. In [11], randomly selected discrete Fourier transform (DFT) columns were used to modulate a spread sequence and generate different beams to obtain channel measurements in different sectors. In [18], a contiguous band of directions is illuminated by sub-arrays. Then, the beam at each sub-array is phase modulated to construct an ensemble of in-sector beams. In [19], the beams were sampled from a large set of random codes based on their capability to focus energy on a sector of interest. We will show, by simulations, that the techniques in [11], [18], and [19] result in poor in-sector channel estimates than our method. In [20], linear convolution at the output of a fully digital array is performed, and the steady-state output of the digital array is decimated to reduce the number of measurements and achieve parallel processing. Our method, unlike [20], performs circular convolution that preserves the channel dimension and obtains compressive measurements of the channel without needing to discard measurements. In [22] and [23], an adaptive beamforming algorithm based on sequential search is proposed to reduce the beam scanning time while combating the low SNR issue in initial access. The methods in [22] and [23] only support wireless channels with a single dominant path, while our method exploits sparsity and can support channels with multiple paths.

In this paper, we adopt a two-stage approach for beamforming. In the first stage, the compressive measurements of the channel within the best sector are used to estimate the channel within this sector. Next, the estimated in-sector channel is used to perform conjugate beamforming. We propose a new approach for in-sector channel estimation by solving two main challenges. First, how to design beams that focus the transmitted energy on distinct non-overlapping sectors within the beamspace. We will see that this problem is extremely challenging with low-resolution phased arrays. Second, how to optimize the compressed sensing (CS) matrices to achieve low CS aliasing artifacts in the in-sector channel estimate. We solve both these problems by constructing new in-sector beams, such that the corresponding antenna weight matrices (AWMs) can be applied in low-resolution phased arrays. These AWMs, referred to as base AWMs, each focus power on a distinct sector. In our method, the channel measurements for CS within the sector of interest are then obtained during BRP by circularly shifting the base AWM. Our main contributions are listed below.

- We propose a beam codebook for SLS that results in a higher received power than existing codebooks. The designed beams have a comb-like structure and illuminate distinct non-overlapping sectors in the beamspace. The AWMs associated with our beams can be realized with phase shifters whose resolution scales logarithmically with the number of sectors.
- We construct a CS matrix by optimizing the sequence of circular shifts applied to the base AWM to acquire channel measurements within the sector of interest. We show

that the optimized shifts result in lower aliasing artifacts in CS when compared to the use of random circular shifts.

- We study support recovery and in-sector channel reconstruction guarantees for CS using the orthogonal matching pursuit (OMP) algorithm. Our study investigates how imperfections in the designed sectors impact the in-sector channel estimate. We show, by simulations, that our in-sector CS technique results in a lower channel reconstruction error and a higher achievable rate than comparable benchmarks.

We would like to highlight that the emphasis of this paper is on designing CS matrices for in-sector channel estimation and not on the development of a CS algorithm.

We explain how the comb-like beam patterns proposed in our paper differ from the multi-fingered illumination patterns proposed in [24] and [25]. The antenna weights corresponding to the multi-fingered beam patterns are constructed by taking the DFT of pseudo-random binary vectors [24], or deterministic vectors drawn from DeVore’s binary matrices [25]. Implementing the antenna weights in [24] and [25], however, requires both magnitude and phase control at the array, leading to more complex hardware than a phased array. Our proposed comb-like beam patterns require only phase control at the antenna array. Furthermore, the concept of circular shifting in [25] was used in the beamspace to illuminate different sections in the angle domain. In our paper, the circular shifts are applied to the antenna domain AWMs resulting in beam patterns that all illuminate the same sector. Our proposed circular shifts are also optimized to achieve low aliasing artifacts within the sector, unlike [25] that uses linear circular shifts.

The techniques in [11], [14], and [26], along with our method, fall within the umbrella of convolutional CS (CCS) [27], where circular shifts of a code are employed to acquire CS measurements. We now discuss how our paper distinguishes itself from prior work on CCS-based channel estimation or beam acquisition. The work in [14] and [26] employed perfect binary arrays and Zadoff-Chu codes as base AWMs, and used random circular shifts of these AWMs to acquire CS measurements. The AWMs in [14] and [26] generate quasi-omnidirectional beams, which result in poor SNR in the channel measurements. Furthermore, the random circular shifts used in [14] and [26] result in uniformly spread aliasing artifacts, which is also undesirable when estimating the channel within a sector.

In our recent paper [1], we developed an in-sector CCS-based channel estimation technique, assuming a uniform linear array at the transmitter. We assumed infinite resolution amplitude and phase control in [1] to construct contiguous sectors. Our solution in [1], however, cannot be realized in phased arrays which allow only finite-resolution phase control. We also designed a sub-sampling scheme in [1] to push aliasing artifacts outside contiguous sectors realized with linear antenna arrays. Extending our solution in [1] to a planar array is beyond the scope of this work. In this paper, we address the practical limitations in [1] by designing a new comb-like codebook, and develop a 2D subsampling method that is best suited for this codebook. To study the impact of

TABLE I
ABBREVIATIONS USED IN THE PAPER

Abbreviation	Description
AWM	Antenna weight matrix
BRP	Beam refinement protocol
CCS	Convolutional CS
OMP	Orthogonal matching pursuit
PCS	Proposed circular shifts
PSF	Point spread function
RCS	Random circular shifts
SLS	Sector level sweep
STF	Short training field
TRN	Training

imperfections in the designed codebook on sparse recovery, we use our result in [2] on the analysis of the OMP when the columns of a CS matrix have different norms. This paper discusses the application of our result in [2] for the channel estimation problem.

Notation: We use a , \mathbf{a} and \mathbf{A} to denote a scalar, vector, and a matrix. The indexing of vectors and matrices begins at 0. \mathbf{a}_i is the i^{th} column of \mathbf{A} . We denote the $(i, j)^{\text{th}}$ entry of \mathbf{A} by A_{ij} or $A(i, j)$. The ℓ_2 norm of \mathbf{a} is denoted by $\|\mathbf{a}\|_2$. We use $\|\mathbf{A}\|_F$ to denote the Frobenius norm of \mathbf{A} and we use $|\mathbf{A}|$ to denote a matrix that contains the element-wise magnitudes of \mathbf{A} . For an integer N , we define the set $[N] = \{0, \dots, N-1\}$. Also, $\langle i \rangle_N$ is the modulo- N remainder of i . We use $(\cdot)^T$, $(\cdot)^c$ and $(\cdot)^*$ to denote the transpose, conjugate and conjugate-transpose operators. We define the vector version of \mathbf{A} as $\text{vec}(\mathbf{A}) = [\mathbf{a}_0^T, \dots, \mathbf{a}_{N-1}^T]^T$. We define $\text{Diag}(\mathbf{a})$ to be a diagonal matrix with \mathbf{a} on its diagonal. We use \circledast , \otimes , and \odot to denote the circular convolution, the Kronecker product, and the Hadamard product. The inner product of \mathbf{A} and \mathbf{B} is $\langle \mathbf{A}, \mathbf{B} \rangle = \sum_{i,j} A_{ij} B_{ij}^c$. Finally, $\mathcal{CN}(0, \sigma^2)$ is the zero-mean complex Gaussian distribution with variance σ^2 and $\mathbf{j} = \sqrt{-1}$. In Table I, we provide a list of all the abbreviations used in the paper.

II. CHANNEL AND SYSTEM MODEL

In this section, we consider a narrowband point-to-point wireless system to explain the transmit beam acquisition problem. In section V, we extend our sparse in-sector channel estimation-aided beam acquisition technique to a wideband scenario using the IEEE 802.11ad frame structure.

A. Channel Model

We consider an $N \times N$ half-wavelength spaced uniform planar array at the transmitter (TX) and a single antenna receiver (RX) as shown in Fig. 1(a). We assume isotropic antenna elements at the TX and the RX, for simplicity. In this paper, we consider the transmit beam acquisition problem where only the TX needs to align its beam towards the best direction [8], [14]. This problem differs from the beam alignment problem in which both the TX and RX need to align their beams to create a directional link between them [18], [25]. We would like to

mention, however, that our solution can also be applied to the beam alignment problem by using the designed codebooks at both the TX and the RX. The application of our codebooks is feasible provided that their antenna array dimensions are a power of two. Such array dimensions are commonly used in practical implementations [28], [29], [30], [31]. Extending our solution to other array dimensions is beyond the scope of this paper.

The narrowband multiple-input single-output channel between the TX and RX is modeled as an $N \times N$ matrix \mathbf{H} , the matrix representation of the $N^2 \times 1$ vectorized channel. The channel comprises L propagation rays, where the ℓ^{th} ray has a complex gain of β_ℓ , an azimuth angle-of-departure $\theta_{a,\ell}$ and an elevation angle-of-departure $\theta_{e,\ell}$. By defining the beamspace angles as $\omega_{a,\ell} = \pi \sin \theta_{e,\ell} \sin \theta_{a,\ell}$, $\omega_{e,\ell} = \pi \sin \theta_{e,\ell} \cos \theta_{a,\ell}$ [32] and the $N \times 1$ Vandermonde vector $\mathbf{a}_N(\omega)$ as

$$\mathbf{a}_N(\omega) = [1, e^{j\omega}, e^{j2\omega}, \dots, e^{j(N-1)\omega}]^T, \quad (1)$$

the baseband channel matrix \mathbf{H} is given by

$$\mathbf{H} = \sum_{\ell=1}^L \beta_\ell \mathbf{a}_N(\omega_{e,\ell}) \mathbf{a}_N^T(\omega_{a,\ell}). \quad (2)$$

The channel dimension N^2 can be in the order of hundreds to thousands in typical mmWave or THz access points.

The channel \mathbf{H} is approximately sparse in the angle domain due to high scattering at mmWave and THz wavelengths [4]. To exploit this property during channel reconstruction, \mathbf{H} is expressed in the beamspace (angle domain) where it has a sparse representation. Since we assume a uniform planar array at the TX, the 2D-DFT dictionary is used to represent \mathbf{H} in the beamspace. We use \mathbf{U}_N to denote the standard $N \times N$ unitary DFT matrix and \mathbf{X} to denote the beamspace representation of \mathbf{H} . Then, \mathbf{X} and \mathbf{H} are related as

$$\mathbf{H} = \mathbf{U}_N \mathbf{X} \mathbf{U}_N. \quad (3)$$

In our analysis, we assume that \mathbf{X} is exactly sparse, i.e., the beamspace angles are exactly aligned with any of the N^2 directional 2D-DFT beam directions. In our simulations, we use channels obtained from the NYU channel simulator [33] where \mathbf{X} is only approximately sparse.

B. System Model

The TX uses a phased array wherein the antennas are connected to a single RF chain through a q -bit phase shifter. The set of the possible weights at each antenna is $\mathbb{Q}_q = \{e^{j2\pi\ell/2^q}/N : \ell \in [2^q]\}$. As an example, $\mathbb{Q}_1 = \{1/N, -1/N\}$ can be realized with a 1-bit phased array. The TX can apply AWMs to its phased array, which are constrained to be within $\mathbb{Q}_q^{N \times N}$, i.e., the set of all $N \times N$ matrices with entries in \mathbb{Q}_q . In this paper, the AWMs are designed such that their corresponding beams illuminate only a certain set of indices of the beamspace \mathbf{X} . A *sector* is defined as a group of indices of the beamspace that are illuminated by a beam. We use S to denote the number of sectors used to partition the $N \times N$ beamspace grid into disjoint subsets \mathcal{A}_s , $\forall s \in [S]$. Hence, \mathcal{A}_s denotes the set of all beamspace indices illuminated in

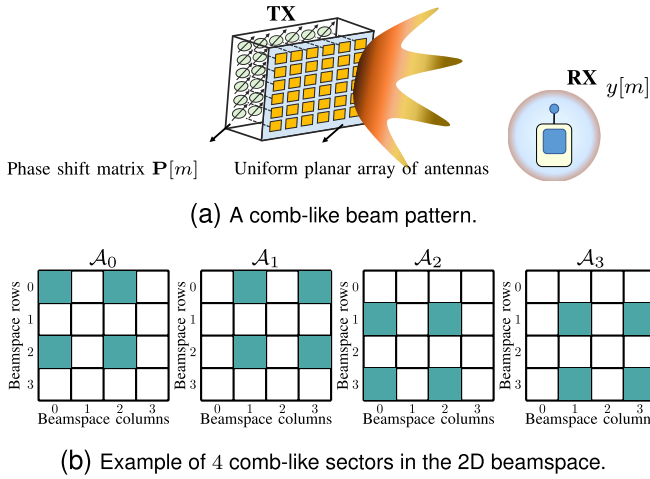


Fig. 1. An mmWave system with a uniform planar array at the TX employing comb-like beams designed in this work. Each comb-like beam illuminates a beamspace sector shown in (b). In this paper, the sector that results in the highest received power is identified, and then the channel within that sector is estimated for beamforming.

sector s . The union of $\{\mathcal{A}_s\}_{s=0}^{S-1}$, i.e., $[N] \times [N]$, spans the entire beamspace. An example of the sectors $\{\mathcal{A}_s\}_{s=0}^{S-1}$ with our comb-like construction proposed in Sec. III is shown in Fig. 1(b) for $S = 4$.

We now explain how our in-sector CS-based beam acquisition method can be integrated into SLS and BRP of the beam training procedure in IEEE 802.11ad/ay [34] standards. We assume a block fading channel and that the channel remains constant throughout the SLS and BRP procedures. This assumption is reasonable in practice for a typical 802.11ad/ay application. For instance, the coherence time is about 1 ms [35] in an indoor setup, while the SLS phase takes about 15.76 μs per sector sweep frame [36] and a BRP packet is of up to 46.96 μs [37, Section 20.12.3].

1) *Sector Level Sweep*: During SLS, the TX uses sector sweep frames and illuminates the channel with sectored beam patterns. The standard, however, does not prescribe specific beam patterns to conduct SLS. These beams may be the common contiguous patterns discussed in [9], [11], and [10] or the comb-like patterns proposed in this work as shown in Fig. 1(b). We define $\{\mathbf{P}_s\}_{s=0}^{S-1}$ as the base AWMs applied at the TX for SLS. The base AWM \mathbf{P}_s illuminates sector s . We use y_s^{slis} to denote the measurement acquired when the TX applies \mathbf{P}_s and $v_s \sim \mathcal{CN}(0, \sigma^2)$ as the noise in this measurement, i.e.,

$$y_s^{\text{slis}} = \langle \mathbf{H}, \mathbf{P}_s \rangle + v_s. \quad (4)$$

In SLS, the RX calculates the received power associated with (4) for each sector. Then, it determines the sector of interest as the one with the highest received power using

$$s_{\text{opt}} = \underset{s \in [S]}{\text{argmax}} |y_s^{\text{slis}}|^2. \quad (5)$$

An illustration of the SLS procedure is shown in Fig. 2.

For sector s , we define the set of beamspace indices \mathcal{A}_s as the locations in the beamspace \mathbf{X} that are illuminated by the base AWM \mathbf{P}_s . To see how \mathcal{A}_s is exactly determined from \mathbf{P}_s , observe that the inner product of two matrices is

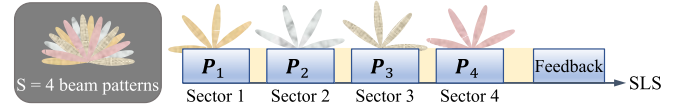


Fig. 2. Example of SLS to determine the sector of interest using $S = 4$ disjoint comb-like sectors designed with our approach. The RX finds the sector of interest s_{opt} as the one that results in the highest received power and feedbacks this information to the TX. The TX can then estimate the channel within the sector using BRP.

the same as the inner product of their inverse 2D-DFTs, i.e., $\langle \mathbf{H}, \mathbf{P}_s \rangle = \langle \mathbf{X}, \mathbf{U}_N^* \mathbf{P}_s \mathbf{U}_N \rangle$. When the TX applies \mathbf{P}_s to its array, it generates a beam that illuminates the beamspace at the indices where $\mathbf{U}_N^* \mathbf{P}_s \mathbf{U}_N$ is non-zero. Therefore, $\mathcal{A}_s = \{(k, \ell) : |(\mathbf{U}_N^* \mathbf{P}_s \mathbf{U}_N)_{k, \ell}| \neq 0\}$. For the identified sector s_{opt} , we define the corresponding base AWM as $\mathbf{P}_o = \mathbf{P}_{s_{\text{opt}}}$ for ease of notation. The corresponding set $\mathcal{A}_o = \mathcal{A}_{s_{\text{opt}}}$. Our objective in codebook design for SLS is to design $\{\mathbf{P}_s\}_{s=0}^{S-1}$ such that each of them illuminates a distinct set of indices in the beamspace, i.e., $\{\mathcal{A}_s\}_{s=0}^{S-1}$ are disjoint and their union is the entire beamspace. The main challenge in the design of such AWMs is due to the constraint that $\mathbf{P}_s \in \mathbb{Q}_q^{N \times N} \forall s$. In Section III, we present our codebook and show that it outperforms those constructed in prior work [9], [10], [11].

SLS uses only the received power to identify the best sector s_{opt} and it does not require estimating the channel \mathbf{H} . The antenna weights obtained at the end of the SLS phase, however, usually do not provide sufficient beamforming gain as $S \ll N^2$. To further improve the beamforming gain, a narrow beam can be formed after estimating the spatial channel within the identified sector. The next subsection explains the main challenges to be solved in estimating the in-sector channel.

2) *Beam Refinement Protocol*: During BRP, the TX applies a collection of AWMs that illuminate directions within the sector of interest. Under the assumption that the S sectors uniformly partition the beamspace, the in-sector channel is an N^2/S dimension vector. A simple approach to estimate this vector is to apply directional beams that exhaustively scan all directions within the sector. Such a scan, however, results in a substantial training overhead, which is in the order of N^2/S . To avoid this high training overhead, we develop an in-sector CS-based method that obtains compressive measurements of the channel within the sector of interest.

We use M to denote the number of CS measurements within the sector s_{opt} . These measurements are obtained using an ensemble of beams $\{\mathbf{P}_o[m]\}_{m=0}^{M-1}$ that only illuminate the sector of interest, i.e., the matrices $\{\mathbf{U}_N^* \mathbf{P}_o[m] \mathbf{U}_N\}_{m=0}^{M-1}$ are non-zero only at the indices in \mathcal{A}_o . For a measurement noise $v[m] \sim \mathcal{CN}(0, \sigma^2)$, the m^{th} in-sector measurement $y[m]$ of the channel is

$$y[m] = \langle \mathbf{H}, \mathbf{P}_o[m] \rangle + v[m]. \quad (6)$$

Our goal for in-sector CS is to construct $\{\mathbf{P}_o[m]\}_{m=0}^{M-1}$ such that: i) $\mathbf{P}_o[m] \in \mathbb{Q}_q^{N \times N}$ illuminates only the directions within \mathcal{A}_o for each m and ii) the collection $\{\mathbf{P}_o[m]\}_{m=0}^{M-1}$ results in a low channel estimation error within the sector of interest. In-sector CS is promising over CS techniques [14], [15], [16], [17] that employ wide beams, because the SNR of the in-sector

measurements is higher than those acquired with a wide beam by about $10 \log_{10} S$ dB, which is the sector gain.

III. PROPOSED SECTORS AND BASE AWMS FOR SLS

SLS is usually performed using beam patterns that illuminate disjoint and complementary sectors within the beamspace. This is because such illumination patterns concentrate the transmitter's power only over a fraction of the beamspace, enabling a higher received SNR for initial access. In the SLS literature [9], [10], and [38], it is common to consider contiguous sectors such as the ones shown in Fig. 3(a). The AWMs that achieve such contiguous patterns, however, cannot be realized with extremely low-resolution phased arrays such as one-bit phased arrays. To see this, let us consider the problem of constructing AWMs that result in illumination patterns shown in Fig. 3(a) using a 4×4 antenna array with one-bit phase shifters. Here, the AWMs need to be chosen from $\{\pm 1\}^{4 \times 4}$ due to the one-bit constraint. As the matrices in $\{\pm 1\}^{4 \times 4}$ are purely real, their inverse 2D-DFTs are mirror symmetric [39], i.e., a pattern that illuminates (k, ℓ) beamspace index must also illuminate the $(\langle -k \rangle_N, \langle -\ell \rangle_N)$ index. We observe that the contiguous patterns in Fig. 3(a) do not exhibit a mirror symmetric pattern. As a result, the sectors shown in Fig. 3(a) cannot be realized in one-bit phased arrays. To address this challenge, in this paper, we design comb-like illumination patterns such as the ones shown in Fig. 3(b). Such comb-like patterns exhibit mirror symmetry, and the corresponding AWMs can be realized with phased arrays whose resolution can be as low as one bit.

A. Proposed Construction for AWMs in SLS

Now, we explain the structure of the proposed comb-like patterns and discuss our method to design the base AWMs $\{\mathbf{P}_s\}_{s=0}^{S-1}$ with entries in $\mathbb{Q}_q^{N \times N}$ to achieve such patterns.

We drop the sector index s to explain the first step in our technique to construct AWMs for SLS. To design comb-like structures in the beamspace, our method constructs an antenna domain building block \mathbf{C} with N_e rows and N_a columns. We assume that both N_e and N_a divide N , and the product $N_e N_a$ is a power of 2. The building block \mathbf{C} is chosen from the 2D-DFT codebook such that it illuminates just one direction in the $N_e \times N_a$ beamspace. An example for \mathbf{C} is shown in Fig. 4(a). With our design, the inverse 2D-DFT of \mathbf{C} , i.e., $\mathbf{U}_{N_e}^* \mathbf{C} \mathbf{U}_{N_a}^*$, has just one non-zero entry and $N_e N_a - 1$ zeros. Next, the matrix \mathbf{C} is upsampled by a factor of N/N_e along the row dimension and by a factor of N/N_a along the column dimension. We define these upsampling factors as

$$\rho_e = N/N_e \text{ and} \quad (7)$$

$$\rho_a = N/N_a, \quad (8)$$

and the upsampled version of \mathbf{C} is defined as $\tilde{\mathbf{C}} \in \mathbb{C}^{N \times N}$. As upsampling a signal results in replication and scaling in the Fourier domain, the beamspace representation of $\tilde{\mathbf{C}}$ is a scaled repetition of the inverse Fourier transform of the building block [40]. This repetitive pattern results in a comb-like structure in the beamspace as shown in Fig. 4.

Now, we summarize the final step in base AWM design to construct a phased array compatible matrix which achieves a comb-like beam pattern. Although the upsampled building block $\tilde{\mathbf{C}}$ results in a comb-like pattern, it cannot be realized with a phased array. This is because $\tilde{\mathbf{C}} \notin \mathbb{Q}_q^{N \times N}$ as it has several zeros. To construct a matrix in $\mathbb{Q}_q^{N \times N}$ that achieves a comb-like pattern, we first make use of the property that circularly shifting a matrix does not change the magnitude of its 2D-DFT. As a result, any 2D-circular shift of $\tilde{\mathbf{C}}$ results in the same illumination pattern as $\tilde{\mathbf{C}}$. We also observe that the locations of the zeros are complementary across all the 2D-circular shifts of $\tilde{\mathbf{C}}$. Our method takes a weighted combination of the $\rho_e \rho_a$ 2D-circular shifts of $\tilde{\mathbf{C}}$ to construct a base AWM in $\mathbb{Q}_q^{N \times N}$. The weights are optimized such that the illumination pattern associated with this weighted combination is almost flat within the designed sector. We will show in Sec. IV-C that such flat profiles achieve a low reconstruction error using our sparse recovery guarantees from [2]. Our design procedure is illustrated in Fig. 4 for a particular sector.

We now explain the mathematical details of our procedure to construct $S = N_a N_e$ sectors. As the entries of the building block are drawn from an $N_e \times N_a$ 2D-DFT codebook, realizing the designed AWMs in a phased array requires $q = \log_2(\max(\{N_a, N_e\}))$ -bit phase shifters. We index the $N_a N_e$ sectors in our design using the 2D-index pair (k_e, k_a) , where $k_e \in [N_e]$ and $k_a \in [N_a]$. The sector index s is expressed as $s = N_a k_e + k_a$. The set of beamspace indices associated with this sector is

$$\begin{aligned} \mathcal{A}_s = \{ (p, q) : p = n N_e + k_e, q = m N_a + k_a, \\ n = [\rho_e], m = [\rho_a] \}, \end{aligned} \quad (9)$$

which can be interpreted as a comb-like pattern anchored at (k_e, k_a) . A detailed description of our method to construct a base AWM \mathbf{P}_s that illuminates \mathcal{A}_s is given below.

- Construct the building block $\mathbf{C}_s \in \mathbb{Q}_q^{N_e \times N_a}$ as an outer product of the k_e^{th} column of \mathbf{U}_{N_e} and the k_a^{th} column of \mathbf{U}_{N_a} , i.e.,

$$\mathbf{C}_s = \mathbf{U}_{N_e}(:, k_e) \mathbf{U}_{N_a}^T(:, k_a). \quad (10)$$

Similar to [14], we define $\mathbf{C}_{s, \text{FC}}$ as the flipped and conjugated version of \mathbf{C}_s . The angle domain matrix associated with the building block is then

$$\mathbf{B}_s = \mathbf{U}_{N_e}^* \mathbf{C}_{s, \text{FC}} \mathbf{U}_{N_a}^* \quad (11)$$

It can be shown that $B_s(k_e, k_a) = 1$ and $B_s(i, j) = 0 \forall (i, j) \neq (k_e, k_a)$.

- Upsample \mathbf{C}_s by a factor of ρ_e along the columns and ρ_a along the rows. The upsampled matrix is obtained by first inserting $\rho_e - 1$ zero-valued row vectors between successive rows of \mathbf{C}_s , and then inserting $\rho_a - 1$ zero-valued column vectors between successive columns of the resultant matrix. The upsampled result is an $N \times N$ matrix $\tilde{\mathbf{C}}_s$, whose beamspace representation is defined as

$$\tilde{\mathbf{Z}}_s = \mathbf{U}_N^* \tilde{\mathbf{C}}_{s, \text{FC}} \mathbf{U}_N^* \quad (12)$$

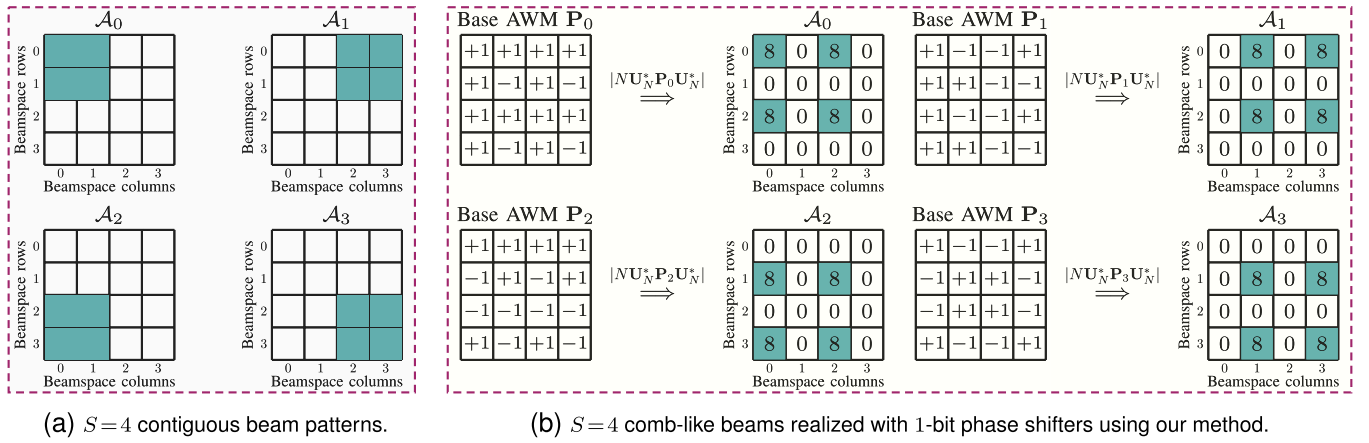


Fig. 3. Contiguous and comb-like beam patterns to illuminate $S=4$ disjoint sections of the 2D beamspace with a 4×4 array at the TX. With 1-bit phase shifters, the AWMs corresponding to the beam patterns in (a) cannot be realized, while those corresponding to the patterns in (b) can be achieved using our construction in Sec. III-A.

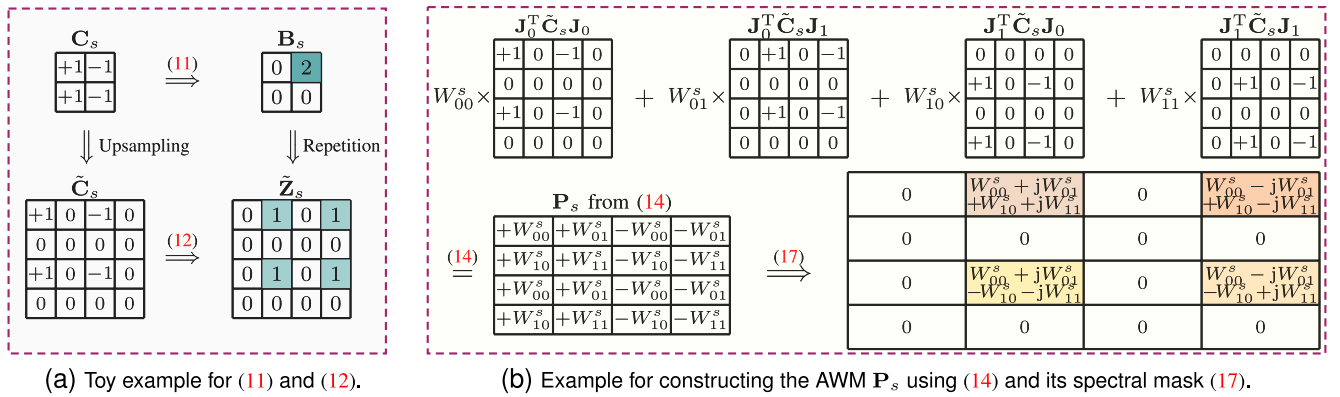


Fig. 4. An example of our proposed framework to construct AWMs that focus energy within sectors with comb-like patterns. Here, $N=4$, the number of sectors are $S=4$, $N_e=2$, and $N_a=2$. Therefore, $\rho_e=2$ and $\rho_a=2$.

$$= \frac{1}{\sqrt{\rho_e \rho_a}} \left\{ \begin{array}{ccc} \text{\scriptsize } \rho_a \text{ times} \\ \mathbf{B}_s & \cdots & \mathbf{B}_s \\ \vdots & \ddots & \vdots \\ \mathbf{B}_s & \cdots & \mathbf{B}_s \end{array} \right\} \rho_e \text{ times.} \quad (13)$$

Here, (12) follows from the upsampling property of the 2D-DFT [41]. Observe that $\tilde{\mathbf{Z}}_s$ exhibits a comb-like structure as it contains repetitions of \mathbf{B}_s , that has a single non-zero entry. The pattern in $\tilde{\mathbf{Z}}_s$, however, cannot be realized in a phased array as its antenna domain representation $\tilde{\mathbf{C}}_s \notin \mathbb{Q}_q^{N \times N}$.

- Express \mathbf{P}_s as a weighted sum of $\rho_e \rho_a$ distinct 2D-circular shifts of $\tilde{\mathbf{C}}_s$. Let $\mathbf{J} \in \mathbb{R}^{N \times N}$ denote a circulant delay matrix with the first row of $(0, 1, 0, \dots, 0)$. The subsequent rows of \mathbf{J} are generated by circularly shifting the previous row by 1 unit. The d circulant delay matrix is then $\mathbf{J}_d = \mathbf{J} \cdot \mathbf{J} \cdots \mathbf{J}$. Then, \mathbf{P}_s in our construction is

$$\mathbf{P}_s = \sum_{\ell=0}^{\rho_e-1} \sum_{m=0}^{\rho_a-1} W_{\ell m}^s \mathbf{J}_\ell^T \tilde{\mathbf{C}}_s \mathbf{J}_m. \quad (14)$$

We constraint the entries of the $\rho_e \times \rho_a$ weight matrix \mathbf{W}^s in (14) to \mathbb{Q}_q so that $\mathbf{P}_s \in \mathbb{Q}_q^{N \times N}$.

A possible choice for \mathbf{W}^s is to set its entries to the elements in \mathbb{Q}_q at random. Although a random choice still illuminates the sector of interest, it does not necessarily lead to a *uniform*

illumination pattern across the directions within the sector. Specifically, the entries of \mathbf{Z}_s within the set \mathcal{A}_s will not necessarily have the same magnitude as we can also notice from the example in Fig. 5(b). In this paper, the weights in \mathbf{W}^s are optimized such that the illumination, i.e., the transmitted power, is almost the same across all the directions within each sector. We will show in Section IV-C that having a flat illumination pattern within a sector results in a tight bound on the reconstruction error of the in-sector channel via CS.

We explain how the weights in \mathbf{W}^s are optimized to achieve an almost flat illumination pattern within the sector s . We define an $N \times N$ matrix

$$\mathbf{T}^s = \sum_{\ell=0}^{\rho_e-1} \sum_{m=0}^{\rho_a-1} W_{\ell m}^s \mathbf{a}_N(2\pi\ell/N) \mathbf{a}_N^T(2\pi m/N), \quad (15)$$

where $\mathbf{a}_N(\omega)$ is the $N \times 1$ Vandermonde vector defined in (1). The beamspace representation of the base AWM \mathbf{P}_s in (14), referred to as the spectral mask \mathbf{Z}_s , is given by

$$\mathbf{Z}_s = N \mathbf{U}_N^* \mathbf{P}_{s,FC} \mathbf{U}_N^* \quad (16)$$

$$= N [\mathbf{T}^s]^\circ \odot \tilde{\mathbf{Z}}_s. \quad (17)$$

We arrive at (17) by first applying flipping and conjugation operations to both sides of (14). Then, we use the property that

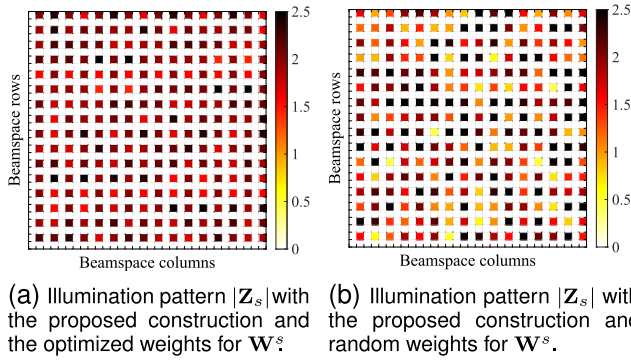


Fig. 5. This figure illustrates the spectral masks of our base AWMs designed for SLS. In this example, we use $N = 32$, $N_e = 2$, $N_a = 2$, $k_e = 0$, $k_a = 1$, and $q = 2$ bits. We observe from Fig. (a) and Fig. (b) that using the optimized \mathbf{W}^s in our comb-like construction results in a more uniform illumination pattern than random weights. Here, $\max_{(i,j) \in \mathcal{A}_s} |Z_{s,ij}| / \min_{(i,j) \in \mathcal{A}_s} |Z_{s,ij}|$ is about 1.78 for the pattern in Fig. (a) and is 8.67 for the pattern in Fig. (b).

circularly shifting a matrix is equivalent to modulation in the Fourier domain. Next, we observe from (13) that $\tilde{\mathbf{Z}}_s$ has equal magnitude entries within the sector s by our construction. For the base AWM \mathbf{P}_s to achieve a uniform illumination over \mathcal{A}_s , we notice from (17) that the entries of \mathbf{T}^s must have the same magnitude over \mathcal{A}_s . We define $\mathbf{T}_{\mathcal{A}_s}^s$ as the $\rho_e \times \rho_a$ submatrix of \mathbf{T}^s , comprising entries from \mathbf{T}^s at the indices in \mathcal{A}_s . Further, we define an $N \times N$ diagonal matrix $\mathbf{D}_N(\omega) = \text{Diag}(\mathbf{a}_N(\omega))$ that contains the $N \times 1$ Vandermonde vector (1) on its diagonal. Then, we can rewrite (15) as

$$\mathbf{T}_{\mathcal{A}_s}^s = \mathbf{U}_{\rho_e}^* \mathbf{D}_{\rho_e}(2\pi k_e/N) \mathbf{W}^s \mathbf{D}_{\rho_a}(2\pi k_a/N) \mathbf{U}_{\rho_a}^*. \quad (18)$$

The weight matrix $\mathbf{W}^s \in \mathbb{Q}_q^{\rho_e \times \rho_a}$ should be optimized such that $\mathbf{T}_{\mathcal{A}_s}^s$, i.e., the magnitude of the inverse DFT of $\mathbf{D}_{\rho_e}(2\pi k_e/N) \mathbf{W}^s \mathbf{D}_{\rho_a}(2\pi k_a/N)$ is flat. We can thus write the optimization problem for designing \mathbf{W}^s as

$$\mathcal{O} : \underset{\mathbf{W}^s \in \mathbb{Q}_q^{\rho_e \times \rho_a}, |\mathbf{V}|=1}{\text{minimize}} \quad \|\mathbf{T}_{\mathcal{A}_s}^s - \mathbf{V}/\sqrt{\rho_e \rho_a}\|_{\text{F}}. \quad (19)$$

The above optimization problem makes sure that the magnitude of entries of $\mathbf{T}_{\mathcal{A}_s}^s$ are as close as possible to $1/\sqrt{\rho_e \rho_a}$ while $\mathbf{W}^s \in \mathbb{Q}_q^{\rho_e \times \rho_a}$. To solve (19), we use an alternating minimization approach similar to the PeCAN algorithm proposed in [42]. In the example shown in Fig. 5, we observe that the magnitude profile of the spectral mask $|\mathbf{Z}_s|$ with the optimized weights has a more uniform illumination within the sector than the one that uses random weights.

In Fig. 6, we compare the received signal strength after SLS using the proposed comb-like sector codebook with those in [9], [11], and [10]. The AWMs in [9], [11], and [10] have contiguous beam patterns, and to meet the low-resolution constraint of the phase shifters, we have quantized the corresponding AWMs when necessary. Due to the comb-like structure of our sectors, the indices in \mathcal{A}_s are different with our design and the benchmarks. The received SNR after SLS is proportional to the received power in the best estimated sector. We observe from Fig. 6 that our proposed AWMs achieve a higher received power after SLS than the other methods. This is because our comb-like sectors are able to concentrate the transmitter's energy perfectly within the sectors without any

leakage, unlike the other methods that suffer due to coarse phase quantization. To measure the power leakage with a codebook, we first define PL_s as the power leakage with AWM \mathbf{P}_s outside \mathcal{A}_s . The leakage $\text{PL}_s = 1 - (\|\mathbf{Z}_s\{\mathcal{A}_s}\|_{\text{F}}^2 / \|\mathbf{Z}_s\|_{\text{F}}^2)$, where $\mathbf{Z}_s\{\mathcal{A}_s}\}$ is a submatrix of the spectral mask \mathbf{Z}_s at the indices in \mathcal{A}_s . The power leakage associated with a codebook is then $\text{PL} = (1/S) \sum_{s=1}^S \text{PL}_s$. For the codebook in [10], Fig. 7 shows the power leakage PL for different resolutions of a 32×32 phased array. Although the set \mathcal{A}_s in our design differs from that in [10], both sets contain the same number of indices to ensure a fair comparison in Fig. 7. We observe from Fig. 7 that the construction in [10] results in considerable power leakage outside the sectors while our method achieves $\text{PL} = 0$ by construction. It is important to highlight that our design requires a resolution of at least $\log_2(\max\{N_a, N_e\})$ bits at the phase shifters, where N_a and N_e are such that the number of sectors $S = N_a N_e$. After the sector of interest is found using SLS, the TX performs in-sector CS-based channel estimation within this sector for beam acquisition.

IV. IN-SECTOR COMPRESSED SENSING FOR CHANNEL ESTIMATION USING THE BRP

To achieve the full beamforming gain of $10 \log_{10} N^2$, the TX needs to further refine the AWM within the sector s_{opt} . This beam refinement can be performed after estimating the N^2/S dimension in-sector channel. In this section, we explain how two-dimensional (2D) CCS (2D-CCS) can be used to acquire channel measurements within the sector s_{opt} . Then, we discuss how to construct an ensemble of AWMs $\{\mathbf{P}_o[m]\}_{m=0}^{M-1}$ that all focus on the sector s_{opt} . Finally, we provide details on the subset of AWMs optimized to reduce aliasing artifacts in CS within the sector.

A. Preliminaries on 2D-CCS

At the end of SLS, the TX can apply \mathbf{P}_o to illuminate the beamspace indices in \mathcal{A}_o , i.e.,

$$\mathcal{A}_o = \{(p, q) : (\mathbf{U}_N^* \mathbf{P}_o \mathbf{U}_N)_{pq} \neq 0\}. \quad (20)$$

The use of \mathbf{P}_o at the TX, however, results in a single spatial channel measurement, which is insufficient to estimate the N^2/S entries of the beamspace in \mathcal{A}_o . To estimate these entries, multiple AWMs that all focus on the same sector must be designed and applied at the TX. One way to construct such AWMs is to circularly shift \mathbf{P}_o and obtain possibly distinct AWMs. This approach works for in-sector CS because circularly shifting a matrix does not change the magnitude of its 2D-DFT [39]. The resulting method in which the TX applies circular shifts of an AWM for the RX to acquire channel measurements is called 2D-CCS [14]. Hence, with 2D-CCS, the M in-sector channel measurements $\{y_o[m]\}_{m=0}^{M-1}$ are obtained by applying M distinct circular shifts of \mathbf{P}_o at the TX during BRP.

Now, we discuss mathematical preliminaries on 2D-CCS [43]. With 2D-CCS, the TX can possibly apply N^2 different 2D-circular shifts of \mathbf{P}_o for in-sector channel estimation. As applying all possible circular shifts results in a substantial measurement overhead, the TX only applies $M <$

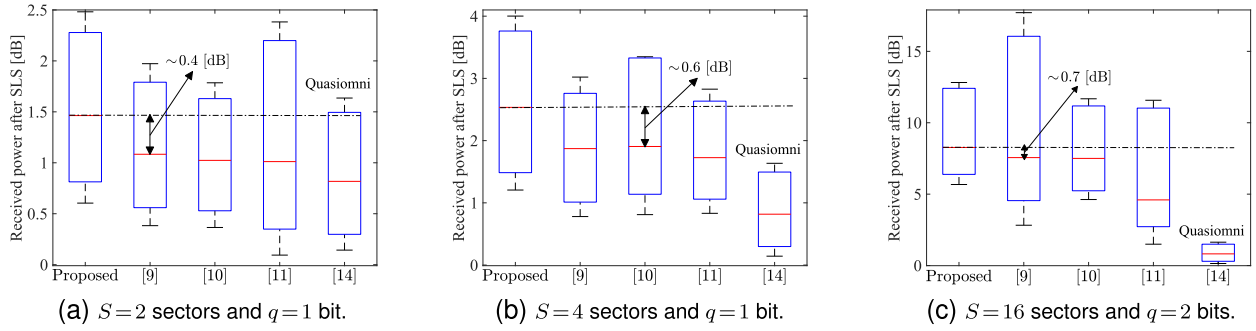


Fig. 6. Our designed base AWMs achieve a higher median received power after SLS than the ones in [9], [11], and [10] and the quasi-omnidirectional beams in [14]. The benchmarks perform poor for low-resolution phase shifters because their AWMs cannot focus the transmitter's power well within the contiguous sectors. Our AWMs focus power exactly within the comb-like sectors by construction. These plots are obtained for a 32×32 array at the TX. The received power is computed for 100 channel realizations from the NYU channel simulator at 60 GHz and $\sigma^2 = 0$. For $\sigma^2 \neq 0$, the performance of our proposed comb-like illumination pattern relative to other methods will remain the same.

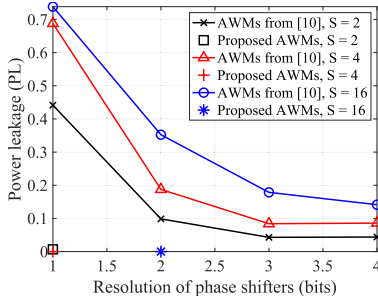


Fig. 7. For a 32×32 phased array, the plot shows that the codebook in [10] results in power leakage outside the defined sectors while our design results in zero leakage. Our codebook can be constructed when the resolution of the phase shifters is at least $\log_2(\max\{N_a, N_e\})$, where the number of sectors can be factorized as $S = N_a N_e$.

N^2 of these circular shifts to obtain channel measurements. These measurements are used together with a sparse prior for channel estimation. As the AWMs in 2D-CCS are all circular shifts of the base AWM \mathbf{P}_o , the channel measurements can be interpreted as a subsampled circular convolution of the channel and \mathbf{P}_o [14]. We use $\Omega = \{(r[m], c[m])\}_{m=0}^{M-1}$ to denote the set of M circular shifts of \mathbf{P}_o applied at the TX to acquire the in-sector channel measurements. Specifically, $\mathbf{P}_o[m]$ is constructed by circularly shifting \mathbf{P}_o by $r[m] \in [N]$ units along its rows, and then circularly shifting the result by $c[m] \in [N]$ units along its columns. We use $\mathbf{H} \circledast \mathbf{P}_o$ to denote the 2D-circular convolution [41] of \mathbf{H} and \mathbf{P}_o . We define $\mathcal{P}_\Omega(\mathbf{A})$ as the subsampling operation that returns a vector of size $|\Omega| \times 1$ containing the entries of \mathbf{A} at the indices in Ω . When the TX applies circulant shifts of \mathbf{P}_o according to Ω , the vector of M in-sector channel measurements acquired by the RX is

$$\mathbf{y} = \mathcal{P}_\Omega(\mathbf{H} \circledast \mathbf{P}_o) + \mathbf{v}. \quad (21)$$

We observe that the channel measurements in 2D-CCS are determined by the base AWM \mathbf{P}_o and the set of circular shifts Ω .

We now describe the in-sector sensing structure in (21) by expressing \mathbf{H} and \mathbf{P}_o in the 2D-DFT domain. Similar to (16), the spectral mask \mathbf{Z}_o corresponding to \mathbf{P}_o is defined as

$$\mathbf{Z}_o = N\mathbf{U}_N^* \mathbf{P}_{o,FC} \mathbf{U}_N^*. \quad (22)$$

From (20) and the properties of the 2D-DFT, it can be shown that $Z_o(k, \ell) \neq 0$ if $(k, \ell) \in \mathcal{A}_o$ and $Z_o(k, \ell) = 0$ if $(k, \ell) \notin \mathcal{A}_o$. We define the masked beamspace \mathbf{R}_o as the entry-wise product of the spectral mask \mathbf{Z}_o and the beamspace \mathbf{X} , i.e.,

$$\mathbf{R}_o = \mathbf{X} \odot \mathbf{Z}_o. \quad (23)$$

As \mathbf{Z}_o contains only $|\mathcal{A}_o|$ number of non-zeros, the masked beamspace \mathbf{R}_o in (23) has utmost $|\mathcal{A}_o|$ non-zeros. Under the assumption that $|\mathcal{A}_o| \sim O(N^2)$, \mathbf{R}_o exhibits a sparse structure due to the sparsity in \mathbf{X} . Now, we use the property that the 2D-DFT of the 2D circular convolution of two matrices is equal to the scaled entry-wise product of their 2D-DFTs [41] to rewrite (21) as

$$\mathbf{y} = \mathcal{P}_\Omega(\mathbf{U}_N \mathbf{R}_o \mathbf{U}_N) + \mathbf{v}. \quad (24)$$

We observe from (24) that the channel measurements in 2D-CCS are simply a subsampled 2D-DFT of a sparse masked beamspace. Here, the mask is the discrete beam pattern corresponding to the base AWM \mathbf{P}_o , and the subsampling is performed at the indices in Ω .

Now, we explain how in-sector channel estimation is performed with the 2D-CCS-based measurements. Any algorithm that uses the measurements $\mathbf{y} = \mathcal{P}_\Omega(\mathbf{U}_N(\mathbf{X} \odot \mathbf{Z}_o)\mathbf{U}_N)$ can only estimate the entries of \mathbf{X} at the indices in \mathcal{A}_o , since the spectral mask \mathbf{Z}_o blanks out entries of \mathbf{X} outside \mathcal{A}_o . In this paper, we use the OMP, a greedy CS algorithm, to obtain the beamspace estimate $\hat{\mathbf{X}}_o$ from the M in-sector measurements. The channel estimate within the sector of interest is then $\hat{\mathbf{H}}_o = \mathbf{U}_N \hat{\mathbf{X}}_o \mathbf{U}_N$.

The success of sparse recovery from partial 2D-DFT measurements in (24) depends on the choice of the subsampling indices in Ω . Prior work has demonstrated that subsampling indices chosen at random allow sparse recovery with a high probability [44]. It is also known that random subsampling often results in aliasing artifacts that are almost uniformly spread over the support of the reconstruction, i.e., $[N] \times [N]$ [45]. Many CS algorithms, like the OMP, iteratively cancel the aliasing artifacts to reconstruct the sparse signal. In our in-sector CS problem, a uniformly spread aliasing profile is undesirable because the sparse masked beamspace signal in (24) is non-zero only at the indices in \mathcal{A}_o . To minimize the reconstruction error, the subsampling set Ω should be

constructed such that aliasing artifacts over \mathcal{A}_o are kept small, while the artifacts outside \mathcal{A}_o are not critical since the masked beamspace is known to be zero in those regions. We construct such sets in Sec. IV-B.

B. Proposed Circular Shifts for in-Sector CS

We discuss our procedure to optimize the set of the circular shifts in Ω to reduce the aliasing artifacts within the sector s_{opt} .

To aid our optimization, we write down the partial 2D-DFT-based measurement model, i.e.,

$$\mathbf{y} = \mathcal{P}_\Omega(\mathbf{U}_N(\mathbf{Z}_o \odot \mathbf{X})\mathbf{U}_N) + \mathbf{v}, \quad (25)$$

using (24) and (23). This measurement model is equivalent to a linear measurement model of the $N^2 \times 1$ sparse vector $\mathbf{x} = \text{vec}(\mathbf{X})$. To represent the linear model explicitly, we replace the sampling operator $\mathcal{P}_\Omega(\cdot)$ with an $M \times N^2$ subsampling matrix \mathbf{S} which is equal to 1 at locations in $\{(m, Nc[m] + r[m])\}_{m=0}^{M-1}$ and zero at the remaining locations. Thus, \mathbf{S} consists of exactly $|\Omega| = M$ ones representing the circular shift indices within Ω . We use $\mathbf{z}_o = \text{vec}(\mathbf{Z}_o)$ to denote the $N^2 \times 1$ vector form of the spectral mask \mathbf{Z}_o . The CS matrix that compresses \mathbf{x} to \mathbf{y} can be determined from (25) as

$$\mathbf{A}_o = \mathbf{S}(\mathbf{U}_N \otimes \mathbf{U}_N) \text{Diag}(\mathbf{z}_o). \quad (26)$$

The linear measurement model in (24) can be rewritten as

$$\mathbf{y} = \mathbf{A}_o \mathbf{x} + \mathbf{v}. \quad (27)$$

Note that the set of the circular shifts $\Omega = \{(r[m], c[m])\}_{m=0}^{M-1}$ determines the subsampling matrix \mathbf{S} and therefore the CS matrix \mathbf{A}_o .

The performance of greedy CS algorithms for sparse recovery usually depends on the mutual coherence of the CS matrix [46]. The mutual coherence is simply the maximum of the normalized inner product between the columns of the CS matrix. It was shown in [46] that minimizing the mutual coherence of the CS matrix results in a tight upper bound for the MSE in the sparse estimate. To this end, we optimize the set of the circulant shifts Ω to minimize the mutual coherence of the CS matrix in our problem.

The CS matrix in our problem has a special structure due to our comb-like construction for the sectors. We define $\mathcal{L}_o = \{qN + p : (p, q) \in \mathcal{A}_o\}$ as the set of the 1D indices where the comb-like spectral mask \mathbf{Z}_o is known to be non-zero. Specifically, for the sector of interest s_{opt} , the vectorized spectral mask \mathbf{z}_o is non-zero at the locations in \mathcal{L}_o and zero at the other locations $[N^2] \setminus \mathcal{L}_o$. Therefore, we can equivalently write the measurements (27) as

$$\mathbf{y} = \mathbf{A}_{\mathcal{L}_o} \mathbf{x}_{\mathcal{L}_o} + \mathbf{v}. \quad (28)$$

In (28), $\mathbf{A}_{\mathcal{L}_o}$ is the $M \times \rho_e \rho_a$ submatrix of \mathbf{A}_o obtained by retaining the columns with indices in \mathcal{L}_o , and $\mathbf{x}_{\mathcal{L}_o}$ is a subvector of \mathbf{x} with the indices in \mathcal{L}_o . So, the in-sector CS problem is to estimate this $\rho_e \rho_a = N^2/S$ dimension sparse vector $\mathbf{x}_{\mathcal{L}_o}$ from the M measurements. Also, sparse recovery in our in-sector CS problem (28) depends on the coherence of $\mathbf{A}_{\mathcal{L}_o}$ rather than \mathbf{A}_o .

Now, we use the notion of the point spread function (PSF) in partial 2D-DFT CS problem [45] to aid our optimization of the sampling set Ω . We define the $N \times N$ binary matrix \mathbf{N}_Ω that is 1 at the indices $\Omega = \{(r[m], c[m])\}_{m=0}^{M-1}$ and is zero at other indices. Therefore, \mathbf{N}_Ω has exactly M entries with the value of 1. The corresponding PSF is [14], [45]

$$\text{PSF}_o = \frac{N}{M} \mathbf{U}_N^* \mathbf{N}_\Omega \mathbf{U}_N^*. \quad (29)$$

In a standard partial 2D-DFT CS problem, the coherence of the CS matrix is simply the maximum sidelobe level of the PSF. In our in-sector CS problem, however, only the sidelobes within the sector of interest matter. With our comb-like sectors constructed according to (9), it can be shown that the coherence of the effective CS matrix $\mathbf{A}_{\mathcal{L}_o}$ is

$$\mu_o = \max_{\{(i,j) \in \mathcal{T}\}} |\text{PSF}_o(i,j)|, \quad (30)$$

where $\mathcal{T} = \{(i,j) : i = nN_e, j = mN_a, (n,m) \in [\rho_e] \times [\rho_a] \setminus (0,0)\}$ for any comb-like sector with the set of beamspace indices defined in (9). The maximum sidelobe level of the PSF at the locations in \mathcal{T} determines the mutual coherence of the CS matrix in our in-sector CS problem.

Now, we formulate the coherence minimization problem as

$$\mathcal{P} : \begin{cases} \min_{\mathbf{N}_\Omega \in \{0,1\}^{N \times N}} \max_{(i,j) \in \mathcal{T}} |\text{PSF}_o(i,j)| \\ \text{s.t.} \sum_{(i,j) \in [N] \times [N]} N_\Omega(i,j) = M. \end{cases} \quad (31)$$

The problem \mathcal{P} is non-convex and hard to solve. In Lemma 1, however, we present an optimal solution $\mathbf{N}_\Omega^{\text{Nyq}}$ that achieves $\mu_o = 0$ when $M = \rho_e \rho_a$. This case corresponds to the Nyquist sampling criterion where the number of measurements M is equal to the sector dimension N^2/S . For the sub-Nyquist regime where $M < \rho_e \rho_a$, our randomized subsampling technique just selects M elements at random from the Nyquist sampling set.

Lemma 1: For $M = \rho_e \rho_a$, the matrix $\mathbf{N}_\Omega^{\text{Nyq}}$ corresponding to $\Omega = [\rho_e] \times [\rho_a]$, with ρ_e and ρ_a defined in (7) and (8), is an optimal solution of \mathcal{P} since it achieves $\mu_o = 0$ in (30).

Proof: See Section VII-A. \square

We now discuss the Nyquist sampling criteria for the N^2 dimension channel estimation problem and the N^2/S dimension in-sector channel estimation problem. In the former case, the Nyquist sampling criterion is $M = N^2$ and the optimal solution \mathbf{N}_Ω for \mathcal{P} is an $N \times N$ matrix of all ones corresponding to $\Omega = [N] \times [N]$. The PSF corresponding to $\Omega = [N] \times [N]$ can be shown to be zero at all entries except $(0,0)$. For the in-sector CCS problem with our comb-like sectors, the ideal PSF need not be zero at all these locations to achieve $\mu_o = 0$. Instead, it only needs to be zero at the locations defined by \mathcal{T} in (30). In Lemma 1, we propose a construction for Ω that achieves $\mu_o = 0$ for $M = N^2/S$. This set simply comprises the 2D-coordinates of any $\rho_e \times \rho_a$ contiguous block on the $[N] \times [N]$ grid.

We use $\mathbf{N}_\Omega^{\text{Nyq}}$ to denote the optimal solution of \mathcal{P} when $M = N^2/S$. In the sub-Nyquist regime, i.e., $M < \rho_e \rho_a$, we propose to select M entries from the Nyquist set of circular shifts in Lemma 1, i.e., $[\rho_e] \times [\rho_a]$, uniformly at random without

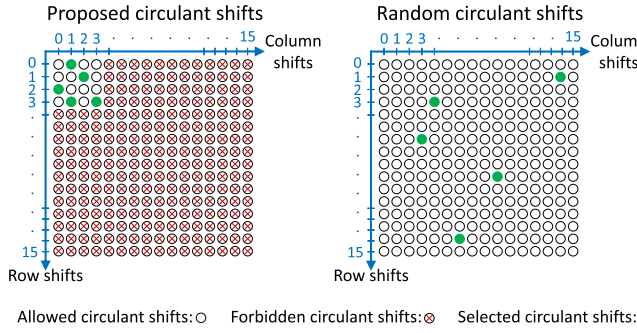


Fig. 8. One realization of the circular shifts chosen in our PCS scheme and the RCS scheme are shown for $N = 16$, $N_e = 4$, $N_a = 4$, $S = N_e N_a$, $\rho_e = N/N_e$, $\rho_a = N/N_a$, and $M = 5$. While the circular shifts in PCS are chosen at random from $\{0, 1, 2, 3\} \times \{0, 1, 2, 3\}$, the shifts in RCS are chosen at random from $[16] \times [16]$.

replacement. We refer to this method as the proposed circular shifts (PCS) for $M < \rho_e \rho_a$, i.e., the subsampling set Ω in PCS is a subset of the optimal set in Lemma 1 for $M = \rho_e \rho_a$. Hence, PCS converges to the optimal solution proposed in Lemma 1 as $M \rightarrow \rho_e \rho_a$. We would like to mention that PCS is different from the fully random circular shifts (RCS) used in [14]. With RCS, the M circular shifts are chosen at random from $[N] \times [N]$, while PCS selects the M shifts at random from $[\rho_e] \times [\rho_a]$ as shown in Fig. 8.

To illustrate the effectiveness of our PCS in the sub-Nyquist regime $M < \rho_e \rho_a$ over RCS, we examine the mutual coherence of the CS matrices. In Fig. 9(a) and 9(b), we compare the entry-wise magnitude of the PSF (29) obtained from PCS and RCS in the Nyquist regime $M = N^2/S$. We observe that with PCS, the PSF is 0 at the indices of interest, i.e., \mathcal{T} , while RCS which selects M indices at random from $[N] \times [N]$ results in a higher coherence μ_o . Next, we plot the cumulative distribution function of μ_o for the two sampling schemes in Fig. 9(c). We notice from the cumulative distribution function that PCS achieves a smaller coherence for the effective CS matrix $\mathbf{A}_{\mathcal{L}_o}$ than RCS. Finally, we show an instance of PCS and RCS in Fig. 8 to distinguish the difference between the two sampling schemes.

C. Guarantees on in-Sector CS With the OMP

In this section, we discuss our guarantees for OMP-based sparse channel estimation within the sector of interest \mathcal{A}_o . Our guarantees are an extension of the coherence-based guarantees in [46], and they help us study the impact of variations in the illumination pattern within the sector. Here, we only provide the main results, and we refer the interested reader to our work in [2] for more details.

Prior work on coherence-based guarantees for the OMP makes a strong assumption that the CS matrix has equal column norms. In our problem, the norms of the columns within the CS matrix in (26) are controlled by \mathbf{z}_o . To express our guarantees as a function of the variations in \mathbf{z}_o , we define $\mathbf{z}_{\mathcal{L}_o}$ as a $\rho_e \rho_a \times 1$ subvector of the vectorized spectral mask \mathbf{z}_o obtained by retaining indices in \mathcal{L}_o . We use d_i to denote the ℓ_2 -norm of the i^{th} column of $\mathbf{A}_{\mathcal{L}_o}$. Using the definition

of \mathbf{A}_o in (26), we can write that

$$d_i = \frac{\sqrt{M}}{N} |z_{\mathcal{L}_o}(i)|, \quad \forall i \in [\rho_e \rho_a], \quad (32)$$

where $z_{\mathcal{L}_o}(i)$ denotes the i^{th} entry of $\mathbf{z}_{\mathcal{L}_o}$. The maximum and the minimum of the column norms in $\mathbf{A}_{\mathcal{L}_o}$ are defined as $d_{\max} = \max_{j \in [\rho_e \rho_a]} d_j$ and $d_{\min} = \min_{j \in [\rho_e \rho_a]} d_j$. As the ℓ_2 -norm of $\mathbf{z}_{\mathcal{L}_o}$ is equal to the Frobenius norm of the AWM \mathbf{P}_o , i.e., 1, we have $\sum_{i=1}^{\rho_e \rho_a} d_i^2 = M/N^2$. Due to this energy constraint,

$$0 < d_{\min} \leq d_{\max} < \sqrt{M}/N. \quad (33)$$

The entries of the spectral mask in $\mathbf{z}_{\mathcal{L}_o}$ are proportional to the norm of the columns of the CS matrix.

Now, we provide performance guarantees to recover the sparse in-sector beamspace $\mathbf{x}_{\mathcal{L}_o}$ from the noisy CS measurements in (27) using the OMP. The guarantees provided in Theorem 1 set an upper bound on the reconstruction error and a lower bound on the probability of successful support recovery depending on the strength of the weakest component of the sparse signal, the noise power, and the sparsity level.

Theorem 1: Let $x_{\mathcal{L}_o, \min} = \min_{j \in \Pi} |x_{\mathcal{L}_o, j}|$, where Π denotes the support of $\mathbf{x}_{\mathcal{L}_o}$ with cardinality $|\Pi| = K$. If

$$d_{\min} x_{\mathcal{L}_o, \min} - (2K - 1) \mu_o d_{\max} x_{\mathcal{L}_o, \min} \geq 2\gamma, \quad (34)$$

for $\gamma > 0$, with probability exceeding

$$\Pr\{E\} \geq \left(1 - \sqrt{\frac{2}{\pi}} \cdot \sqrt{\frac{\sigma}{\gamma}} \exp\left(-\frac{\gamma^2}{2\sigma^2}\right)\right)^{2N^2/S}. \quad (35)$$

the OMP algorithm successfully recovers the support of $\mathbf{x}_{\mathcal{L}_o}$ and the MSE of the estimate $\hat{\mathbf{x}}_{\mathcal{L}_o}$ is upper bounded as

$$\|\hat{\mathbf{x}}_{\mathcal{L}_o} - \mathbf{x}_{\mathcal{L}_o}\|_2^2 \leq \left(\frac{d_{\max}}{d_{\min}}\right)^2 \frac{K\gamma^2}{(d_{\min} - (K - 1)\mu_o d_{\max})^2}. \quad (36)$$

Proof: See Section VII-B. \square

An important insight from Theorem 1 is that the OMP can identify weak coefficients in the beamspace when d_{\max}/d_{\min} of the CS matrix is small. This observation follows by rewriting (34) as

$$x_{\mathcal{L}_o, \min} \geq \frac{2\gamma}{d_{\min} - (2K - 1)\mu_o d_{\max}} \quad (37)$$

$$= \frac{2\gamma/d_{\min}}{1 - \mu_o(2K - 1)(d_{\max}/d_{\min})}. \quad (38)$$

The upper bound on the MSE in (36) monotonically increases with d_{\max}/d_{\min} . In summary, our guarantees on support recovery and the MSE become tight for a small d_{\max}/d_{\min} . We notice from (33) that the smallest possible d_{\max}/d_{\min} is 1. This is achieved when $\min_{i \in [\rho_e \rho_a]} |z_{\mathcal{L}_o}(i)| = \sqrt{S}/N$, equivalently when \mathbf{P}_o uniformly illuminates the sector of interest. These guarantees motivate our optimization objective in (19), which aims to generate AWMs that result in an almost uniform illumination within the sector. Further, it can be concluded from our guarantees that our optimized illumination pattern in Fig. 5(a) should achieve better in-sector channel reconstruction than the pattern in Fig. 5(b).

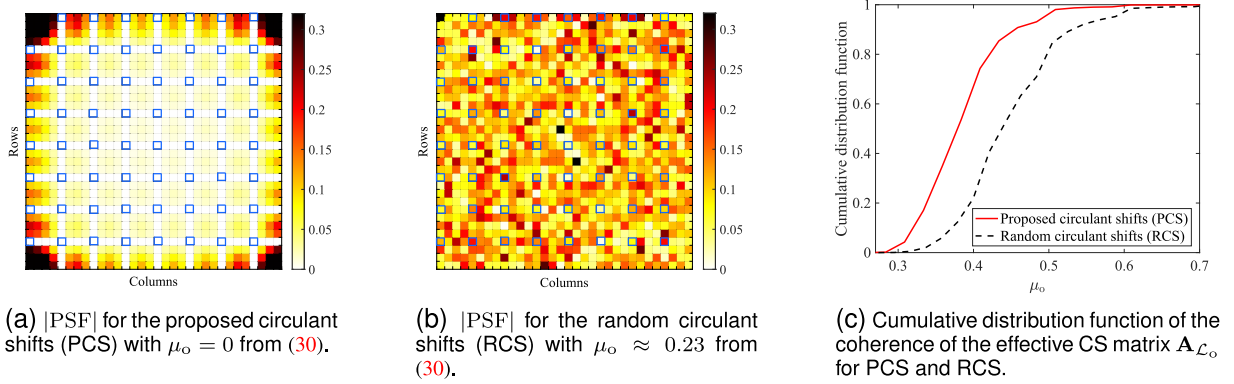


Fig. 9. Proposed subsampling and fully random subsampling for $N = 32$, $N_e = 4$, $N_a = 4$, $S = N_e N_a$, $\rho_e = N/N_e$, $\rho_a = N/N_a$. In (a) and (b), we assume $M = \rho_e \rho_a$ and the entries indicated by \square have indices in \mathcal{T} . The PSF for PCS achieves $\mu_o = 0$, which corresponds to zero aliasing artifacts under Nyquist sampling. For the same number of measurements, however, the PSF with RCS results in a positive μ_o . We observe from (c) that the coherence with PCS is lower than that with RCS in the sub-Nyquist regime for $M = 20$.

V. NUMERICAL RESULTS

In this section, we first describe how the proposed beamforming method is extended to a wideband system using the IEEE 802.11ad frame structure. Then, we discuss the performance of our proposed method in terms of the normalized MSE in the in-sector channel estimate and the achievable rate.

A. Extension to a Wideband System

We denote the L -tap wideband channel as $\{\mathbf{H}[\ell]\}_{\ell=0}^{L-1}$ where $\mathbf{H}[\ell] \in \mathbb{C}^{N \times N}$. The TX first identifies the best sector by applying S different AWMs $\{\mathbf{P}_s\}_{s=0}^{S-1}$ in SLS. The best sector is the one for which the received power, i.e., $\sum_{\ell=0}^{L-1} |\langle \mathbf{H}[\ell], \mathbf{P}_s \rangle + v_\ell|^2$ is the highest and the corresponding base AWM is \mathbf{P}_o . Then, the TX acquires CS measurements within this sector by applying different AWMs $\{\mathbf{P}_o[m]\}_{m=0}^{M-1}$ at the beginning of each training (TRN) subfield in a BRP packet. As shown in Fig. 10, to obtain the m^{th} measurement, at the beginning of the m^{th} TRN subfield, TX sets the antenna weights at the uniform planar array to $\mathbf{P}_o[m]$. With our design, $\mathbf{P}_o[m]$ is a 2D-circular shift of \mathbf{P}_o .

In IEEE 802.11ad, a Golay sequence Ga_{128} of length 128 is used as a guard interval at the beginning of the TRN subfield [47]. This interval provides enough time to change the antenna weights at the TX and also avoids interference across successive subfields. Then, the TX transmits two Golay complementary pairs $\{-\text{Gb}_{128}, \text{Ga}_{128}\}$ and $\{\text{Gb}_{128}, \text{Ga}_{128}\}$ for each AWM, i.e., $\mathbf{P}_o[m]$, applied at the array. The complementary property of Golay sequences can be used to obtain measurements of the equivalent wideband channel seen through the beamformer $\mathbf{P}_o[m]$ [48]. This channel is $\{\langle \mathbf{H}[\ell], \mathbf{P}_o[m] \rangle\}_{\ell=0}^{L-1}$, a vector of length L for each $m \in [M]$. We define $\mathbf{Y}_{\text{blk}} \in \mathbb{C}^{M \times L}$ to denote the set of these ML spatial channel projections within the sector of interest and the measurement noise as $\mathbf{V}_{\text{blk}} \in \mathbb{C}^{M \times L}$. Hence, the $(m, \ell)^{\text{th}}$ entry of \mathbf{Y}_{blk} is

$$Y_{\text{blk}}(m, \ell) = \langle \mathbf{H}[\ell], \mathbf{P}_o[m] \rangle + V_{\text{blk}}(m, \ell). \quad (39)$$

Due to the spreading gain of $N_{\text{seq}} = 256$ with the Golay sequence correlators, the entries of \mathbf{V}_{blk} are independently and independently distributed as $\mathcal{CN}(0, \sigma^2/N_{\text{seq}})$.

In this paper, only the DC subcarrier, i.e., the sum of the L taps of the wideband channel $\mathbf{H}_{\text{sum}} = \sum_{\ell=0}^{L-1} \mathbf{H}[\ell]$ is estimated within the sector of interest. Although our method can be applied to estimate all the taps, we only estimate the sum of the channel taps as it requires less computational complexity than wideband channel estimation. This approach is reasonable because the phased array can only apply a frequency-flat beamformer, which may be designed based on a single subcarrier. The in-sector CS measurements are thus $y[m] = \sum_{\ell=0}^{L-1} Y_{\text{blk}}(m, \ell)$, $\forall m \in [M]$. Now, similar to the narrowband case, in-sector CS can be performed using $\{y[m]\}_{m=0}^{M-1}$ to obtain an estimate of the DC subcarrier $\hat{\mathbf{H}}_{\text{sum}}^o$ within the sector of interest. This estimate can then be used to design the conjugate beamformer at the transmitter to maximize the received power.

B. System Parameters

We consider a 32×32 phased array in Fig. 1(a) at the TX and we assume 1-bit phase shifters unless otherwise stated. The TX-RX distance is 60 m. The heights of the TX and the RX are 3 m and 1.5 m. The system operates at a carrier frequency of 60 GHz with a bandwidth of 100 MHz that corresponds to a symbol duration of 10 ns. We use SNR_{omni} to denote the SNR without spreading gain and without any beamforming gain. This is obtained when the TX applies a quasi-omnidirectional beamformer generated by a perfect binary array [14]. We use mmWave channels obtained from the NYU channel simulator [33] for a line-of-sight scenario in an urban micro environment. For 100 independent channel realizations, the omnidirectional root-mean-square delay spread was less than 25 ns in more than 90% of the channel realizations. We model the wideband channel using $L = 10$ taps corresponding to a duration of 100 ns, which is much larger than 25 ns. The simulation results in this section are averaged over the 100 channel realizations.

C. Performance of the Proposed in-Sector CS-Based Beamforming

We discuss metrics used to evaluate the performance of the proposed method against two other benchmarks. We also

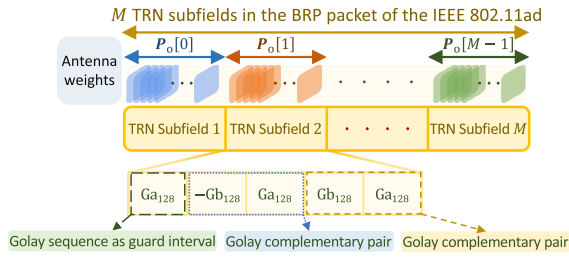


Fig. 10. BRP packet in IEEE 802.11ad may comprise upto 64 TRN subfields containing Golay complementary pairs [37, Table 20-13, Sec. 20.9.2.2.6], [47]. The in-sector CS measurements can be acquired within the sector of interest s_{opt} , when the TX sequentially applies $\{\mathbf{P}_o[m]\}_{m=0}^{M-1}$ at the beginning of each TRN subfield.

assess the performance gain arising from each of our three contributions: (i) Construction of non-overlapping comb-like sectors in SLS, (ii) Optimization of the weight matrix \mathbf{W}^s to achieve an almost uniform illumination pattern, and (iii) Optimization of the circular shifts in PCS for in-sector CS.

To construct the base AWMs in our approach for SLS, we initialize the weight matrix within the iterative optimization algorithm in (19) to different matrices that exhibit good autocorrelation properties. This is done because the algorithm (19) can converge to different local minima depending on the initialization [49]. To this end, we use perfect binary arrays [50], the quantized DFT matrix, the outer product of two Frank sequences [51], the outer product of two Zadoff-Chu sequences [52], and the outer product of two Golomb sequences [53] for the initialization. Then, the initialization that results in the most uniform magnitude profile within our comb-like construction is used to construct a base AWM for the sector.

For CS-based channel estimation within the sector of interest, we used the OMP algorithm [54] to obtain an estimate of \mathbf{H}_{sum} . Assuming that the $(N^2/S) \times 1$ vector $\mathbf{x}_{\mathcal{L}_o}$ in the in-sector CS measurement model (28) is K -sparse with $K \ll \mathcal{O}(N^2/S)$, the computational complexity of the OMP algorithm is dominated by the matrix-vector multiplication $\mathbf{A}_{\mathcal{L}_o}^* \mathbf{y}$ [55]. The partial 2D-DFT structure of the CS matrix $\mathbf{A}_{\mathcal{L}_o}$ in our case, allows fast implementation of $\mathbf{A}_{\mathcal{L}_o}^* \mathbf{y}$ using the fast Fourier transform. It was discussed in [14] that the complexity of each OMP iteration with such a partial 2D-DFT matrix is $\mathcal{O}\left((N^2/S) \log(N/\sqrt{S})\right)$. For a K -sparse signal, OMP requires at most K iterations to converge [46]. Algorithms based on convex optimization can also be used for sparse recovery. One such algorithm, based on the subgradient method, minimizes an ℓ_1 -regularized least squares objective [46]. To achieve ϵ -error in the objective, this method requires $\mathcal{O}(1/\epsilon^2)$ iterations [56]. In our simulations, we observed that the OMP required about 30 iterations, whereas the subgradient method needed several thousand iterations to achieve comparable performance.

We study the performance of 2D-CCS-based with both RCS and the optimized PCS. We note that in RCS, it is possible to have the same measurement equation corresponding to different $\mathbf{P}_o[m]$ s. We remove such measurements to avoid rank deficiency in OMP sparse recovery. Let $\mathbf{H}_{\text{sum}}^o$ denote

the spatially filtered version of \mathbf{H}_{sum} within the sector of interest. The matrix $\mathbf{H}_{\text{sum}}^o$ is obtained by applying a binary mask, that is one at the indices in \mathcal{A}_o , over the beamspace representation of \mathbf{H}_{sum} . We then define the normalized in-sector MSE $\mathbb{E}[\|\mathbf{H}_{\text{sum}}^o - \hat{\mathbf{H}}_{\text{sum}}^o\|_F^2] / \mathbb{E}[\|\mathbf{H}_{\text{sum}}^o\|_F^2]$ as a measure of the reconstruction error in $\mathbf{H}_{\text{sum}}^o$. In addition, we use SNR_{omni} to denote the signal-to-noise ratio when a quasi-omnidirectional beam is used at the TX.

After the in-sector channel is estimated, the TX applies a beamformer $\mathbf{F} \in \mathbb{Q}_q^{N \times N}$ such that $|\langle \mathbf{F}, \hat{\mathbf{H}}_{\text{sum}}^o \rangle|$ is maximized. Let $\text{phase}(\kappa)$ denote the phase of the complex scalar κ . When there is no constraint on the resolution of the phase shifters, i.e., $q = \infty$, from the dual norm inequality [57], $F_{ij}^{\text{opt}} = \exp(j\text{phase}([\hat{H}_{\text{sum}}^o]_{ij})) / N$ is the maximizer of $|\langle \mathbf{F}^{\text{opt}}, \hat{\mathbf{H}}_{\text{sum}}^o \rangle|$. Under q -bit phase quantization, the TX applies $\mathbf{F} = \mathcal{Q}_q(\mathbf{F}^{\text{opt}})$ as the transmit beamformer. The effective wideband single-input single-output channel is then $\{\langle \mathbf{H}[\ell], \mathbf{F} \rangle\}_{\ell=0}^{L-1}$. Finally, we use the *waterfilling* algorithm to obtain the achievable rate associated with the equivalent channel [32].

For the benchmarks, we use the methods from [11], [18], and [19] that use contiguous sectors similar to Fig. 3(a). These sectors are defined by $\mathcal{B}_s = \{(p, q) : k_e \rho_e \leq p < (k_e + 1) \rho_e, k_a \rho_a \leq q < (k_a + 1) \rho_a\}$, each representing a $\rho_e \times \rho_a$ block in the beamspace. The M in-sector CS measurements in [11] are acquired using AWMs that are obtained by modulating a Zadoff-Chu-based sequence with M columns of the 2D-DFT dictionary chosen at random. To construct an AWM that illuminates a contiguous sector, [18] partitions the array into multiple subarrays. Then, it stacks the phase-modulated version of the subarray response vectors and takes the outer product of such vectors to construct the AWM [18]. To construct M different AWMs, the angles used for phase modulation are selected at random such that the resultant AWM focuses on the given sector. For the benchmark in [18], we partition the array into 4 subarrays, a parameter tuned to optimize the method in [18] for our channel dataset. Implementing the AWMs in [11] requires $\log_2 N$ resolution phase shifters and the design in [18] needs infinite-resolution phase shifters, which may not be available in practice. For a fair comparison, we quantize the phase of these codewords to q -bits. For the greedy method in [19], we generate one million AWMs from $\mathbb{Q}_q^{N \times N}$ at random. Then, for each sector in $\{\mathcal{B}_s\}_{s=0}^{S-1}$, we select the top AWM that radiates the largest energy within the sector to be used during the SLS. After determining the sector of interest in SLS, the top M AWMs that radiate the largest energy within the sector of interest are selected to obtain in-sector CS measurements with [19].

In Fig. 11(a), we compare the normalized in-sector MSE of the estimated channel for the proposed in-sector CCS-based method and the benchmarks. We observe a large gap between the proposed method with PCS or RCS and the benchmarks [11], [18], and [19] for a wide range of CS measurements. This is because our AWMs result in a higher received power within the sector of interest, boosting the received SNR and therefore resulting in a low normalized in-sector MSE. The high received power with our method is due

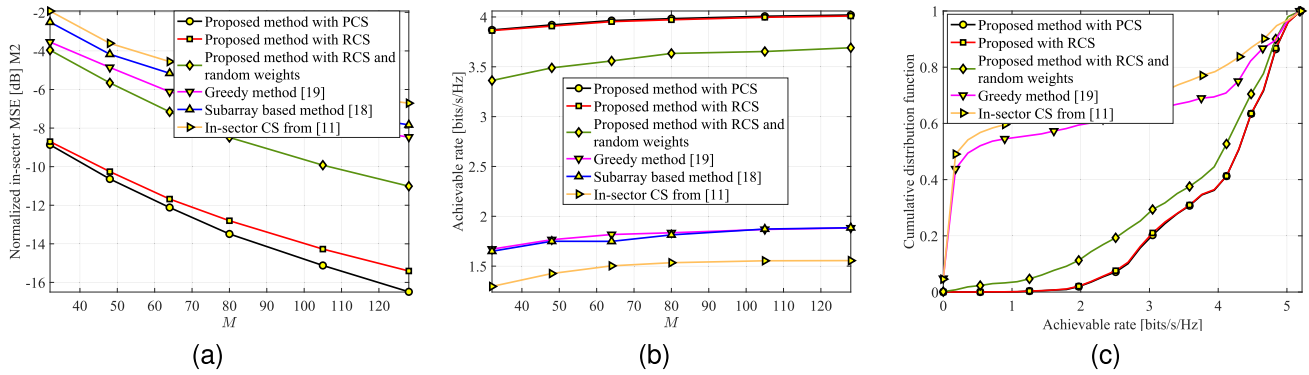


Fig. 11. The plots show the normalized in-sector MSE, achievable rate, and the cumulative distribution function of the achievable rate using the proposed in-sector CCS-based method as well as the benchmarks. We assume $N_e = 2$, $N_e = 2$ which results $S = 4$ sectors. We use $\text{SNR}_{\text{omni}} = -10$ dB. In (c), we use $M = 80$. It can be noticed that the proposed in-sector CCS-based method outperforms the benchmarks when the weight matrix \mathbf{W}^s in (14) is optimized.

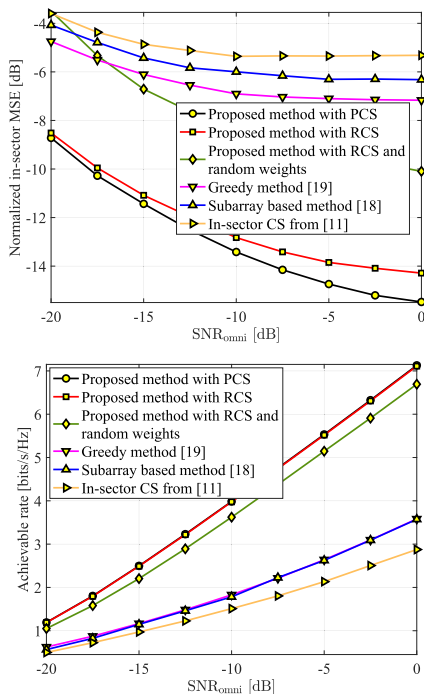


Fig. 12. Here, we consider $N_e = 2$, $N_e = 2$ that correspond to $S = 4$ sectors, and use $M = 80$ in-sector CS measurements. For in-sector CS with our optimized comb-like sectors, we observe that PCS achieves a lower normalized MSE than RCS. This is because the designed set of circular shifts results in lower aliasing artifacts than random shifts. Furthermore, our method outperforms the benchmarks in [11], [18], and [19] in terms of the normalized MSE and the rate.

to the concentration of the transmitter's energy only within the sector, while the AWMs in [11], [18], and [19] result in leakage outside the sector. Also, we observe that our method with PCS results in a lower normalized in-sector MSE than with RCS within the sector of interest. This is because PCS leads to lower aliasing artifacts within the sector of interest than the RCS as we observed in Fig. 9. We can also observe a similar performance difference between our proposed method using PCS or RCS and the benchmarks in the achievable rate from Fig. 11(b) for different CS measurements.

From the cumulative distribution function plot in Fig. 11(c), we observe that with a probability exceeding 0.98, our pro-

posed method with the optimized weight matrix \mathbf{W}^s results in an achievable rate of at least about 2 bits/s/Hz. The use of random weights for \mathbf{W}^s results in a lower rate, which motivates the need to use almost uniform comb-like beams designed in this work. For the other in-sector CS benchmarks based on [11], [18], and [19], we observe that the achievable rate is lower than that with our approach. This is because these methods radiate a significant amount of the transmitter's energy outside their intended sectors.

We observe from Fig. 11(a) that the proposed method with RCS and a random \mathbf{W}^s results in a higher normalized in-sector MSE than the case with the optimized \mathbf{W}^s . This is because a random \mathbf{W}^s is very likely to result in a non-uniform illumination pattern within the comb-like structure as shown in Fig. 5(b). The column norms of such a CS matrix are substantially different with such an illumination, which is expected to result in poor reconstruction according to our analysis in Section IV-C.

In Fig. 12, we compare the proposed in-sector CS method against the benchmarks for different values of SNR_{omni}. We observe that our method outperforms the benchmarks over a wide range of SNR_{omni}. Furthermore, it is evident that at high SNR_{omni}, PCS outperforms RCS due to a significantly lower in-sector normalized MSE in the channel estimate. While at low SNR levels, additive white Gaussian noise remains the dominant factor, at high SNR levels, the aliasing artifacts arising from subsampling in CS dominate. As the aliasing artifacts with PCS are substantially lower than RCS due to the optimized circular shifts, the disparity in performance between PCS and RCS is discernible at high SNR.

VI. ADDRESSING IMPLEMENTATION CHALLENGES WITH OUR IN-SECTOR BEAM ACQUISITION TECHNIQUE

A key assumption in this work is that the received SNR within the best sector is sufficient enough for packet detection. This is reasonable due to the sector gain and the use of low modulation and coding schemes (MCS) such as MCS level 0 during initial access. The RX reports the best identified sector through a sector-sweep feedback packet, which also employs a low modulation and coding scheme [34], [58].

We also assume that perfect timing and carrier synchronization are maintained throughout the process of acquiring in-sector channel measurements within a BRP packet. This synchronization can be established using the *short training field* (STF) at the beginning of a BRP packet in the IEEE 802.11ad standard. In this paper, we ignore the phase jitter and timing drift within a BRP packet. Extending our work to account for such jitters and drifts is beyond the scope of this paper.

We discuss how our technique explained for a single user can be extended to a multi-user setting. As we assume a single RF chain in this paper, the direct application of our sector sweep method to a multi-user setting results in a substantial overhead. This is because the BRP procedure must be performed for different sectors, considering that the best sector varies across the users. This procedure does not scale well with the number of users and can be time-consuming, given that the maximum duration of a BRP packet is 46.96 μs [37, Sec. 20.11.3]. To address this problem, a hybrid beamforming architecture may be used at the TX. In this case, the IEEE 802.11ay standard can be adopted such that different base AWMs can be simultaneously applied across multiple RF chains [58].

Finally, we briefly discuss how our framework can be extended for two types of hybrid beamforming architectures, i.e., (i) fully connected architecture where each RF chain is connected to all the antennas and (ii) subarray-based architecture where each RF chain is connected to a distinct subset of antennas. With fully connected architectures, each RF chain can be used to illuminate a certain sector and the RF chains collectively can illuminate the entire beamspace. This can be achieved by transmitting orthogonal time-domain codes from different RF chains. For the subarray-based architecture, our compressive in-sector channel estimation framework can be applied to each subarray independently. When non-stationarity effects can be ignored, the associated beamspace submatrices of the subarrays share a common support. In such case, sparse recovery algorithms based on dynamic compressed sensing [59] can be used to exploit the common support structure across beamspace submatrices.

VII. CONCLUSION

In this paper, we proposed a new comb structured codebook for sector level sweep with phased arrays. We also developed a CCS-based method for channel estimation or beam acquisition within the sector of interest. Our approach requires a lower training overhead than the classical exhaustive beam scanning methods and integrates well into the beam refinement protocol of the IEEE 802.11ad/ay standards. Furthermore, it overcomes the poor received SNR issue with CS techniques employing wide beams, by concentrating the transmitter's energy in the sector of interest. We also optimized the CS matrix by designing the circular shifts in CCS to reduce the in-sector channel reconstruction error. Finally, we provided conditions that guarantee the successful recovery of the support of beamspace within the sector of interest. Our results indicate that the reconstruction error in the estimated in-sector channel is low when the antenna weights applied at the transmitter illuminate the sector almost uniformly.

APPENDIX

A. Proof of Lemma 1

Let $\mathbf{1}_{\rho_e \times \rho_a}$ denote a $\rho_e \times \rho_a$ all-ones matrix. We use $\Gamma(\omega_1, \omega_2)$ to denote the 2D discrete-space Fourier transform of $\mathbf{1}_{\rho_e \times \rho_a}$ where $\{\omega_1, \omega_2\} \in [0, 2\pi]$ [39] are continuous. The inverse 2D-DFT of $\mathbf{1}_{\rho_e \times \rho_a}$ is $\mathbf{U}_{\rho_e}^* \mathbf{1}_{\rho_e \times \rho_a} \mathbf{U}_{\rho_a}^* = \sqrt{\rho_e \rho_a} \mathbf{E}_{\rho_e \times \rho_a}$ where the $\rho_e \times \rho_a$ matrix $\mathbf{E}_{\rho_e \times \rho_a}$ is zero at all entries except $E_{\rho_e \times \rho_a}(0, 0) = 1$. Hence, we have [39, Sec. 5.5]

$$\frac{1}{\sqrt{\rho_e \rho_a}} \Gamma^* \left(\frac{2\pi i}{\rho_e}, \frac{2\pi j}{\rho_a} \right) = \sqrt{\rho_e \rho_a} E_{\rho_e \times \rho_a}(i, j), \quad \forall (i, j) \in [\rho_e] \times [\rho_a]. \quad (40)$$

Since $E_{\rho_e \times \rho_a}(i, j) = 0 \quad \forall (i, j) \in [\rho_e] \times [\rho_a] \setminus (0, 0)$, from (40), we have

$$\Gamma \left(\frac{2\pi i}{\rho_e}, \frac{2\pi j}{\rho_a} \right) = 0, \quad \forall (i, j) \in [\rho_e] \times [\rho_a] \setminus (0, 0). \quad (41)$$

Next, we observe that $\mathbf{N}_{\Omega}^{\text{Nyq}}$ defined in Lemma 1 is an extended version of $\mathbf{1}_{\rho_e \times \rho_a}$ obtained by appending $\rho_e(N_e - 1)$ zeros at the end of each row and then appending $\rho_a(N_a - 1)$ zeros at the end of each column. Now, we use the fact that the 2D discrete-space Fourier transform $\Gamma(\omega_1, \omega_2)$ of the zero-padded signal remains the same, however, its 2D-DFT will be a densely sampled version of $\Gamma(\omega_1, \omega_2)$ [39, Ch. 5]. Hence, the PSF (29) of $\mathbf{N}_{\Omega}^{\text{Nyq}}$ which is a zero-padded version of $\mathbf{1}_{\rho_e \times \rho_a}$ can be written as

$$\text{PSF}(i, j) = \frac{1}{M} \Gamma^* \left(\frac{2\pi i}{N}, \frac{2\pi j}{N} \right), \quad (i, j) \in [N] \times [N]. \quad (42)$$

Finally, from $N = \rho_e N_e$, $N = \rho_a N_a$ and (41), we observe that $\text{PSF}(i, j) = 0$ at the desired locations defined by \mathcal{T} in (30). Hence, for $\mathbf{N}_{\Omega}^{\text{Nyq}}$, the coherence defined in (30) is equal to zero. Therefore, the sampling set Ω given in the lemma is optimal which concludes the proof.

B. Proof of Theorem 1

To find a guarantee for successful support recovery, we analyze the support detection step in the OMP algorithm [54]. An extended version of this proof is available in our conference paper [2]. We, however, include an outline of this proof here for completeness.

Let $(\mathbf{a}_{\mathcal{L}_o})_j$ denote the j^{th} column of the effective CS matrix $\mathbf{A}_{\mathcal{L}_o}$ in the in-sector CS measurement model (28). The noise term $(\mathbf{a}_{\mathcal{L}_o})_j^* \mathbf{v}/d_j$ in the support detection step of the OMP algorithm can lead to incorrect support detection. Therefore, to control support misdetection under noise, we first examine the event

$$E = \left\{ \max_{j \in [\rho_e \rho_a]} \frac{|(\mathbf{a}_{\mathcal{L}_o})_j^* \mathbf{v}|}{d_j} < \gamma \right\}, \quad (43)$$

where $\gamma := \sigma \sqrt{2(1 + \alpha) \log(N^2/S)}$ and $\alpha > 0$ [46]. In Lemma 2, we provide an upper bound for the probability of occurrence of event E .

Lemma 2: The probability that event E in (43) occurs is lower bounded by

$$\Pr\{E\} \geq \left(1 - \sqrt{\frac{2}{\pi}} \cdot \sqrt{\frac{\sigma}{\gamma}} \exp\left(-\frac{\gamma^2}{2\sigma^2}\right) \right)^{2N^2/S}. \quad (44)$$

Proof: We split $(\mathbf{a}_{\mathcal{L}_o})_j^* \mathbf{v}$ into its real part $\Re((\mathbf{a}_{\mathcal{L}_o})_j^* \mathbf{v})$ and its imaginary part $\Im((\mathbf{a}_{\mathcal{L}_o})_j^* \mathbf{v})$. Since the entries of \mathbf{v} are independently distributed as $\mathcal{CN}(0, \sigma^2)$, the random variables $\{\Re((\mathbf{a}_{\mathcal{L}_o})_j^* \mathbf{v})/d_j\}$ and $\{\Im((\mathbf{a}_{\mathcal{L}_o})_j^* \mathbf{v})/d_j\} \forall j \in [N^2/S]$ are jointly Gaussian and each distributed as $\mathcal{N}(0, \sigma^2/2)$. For any $\kappa \in \mathbb{C}$, we notice that $|\kappa| < \gamma$ whenever $\Re(\kappa) < \gamma/\sqrt{2}$ and $\Im(\kappa) < \gamma/\sqrt{2}$. Using this observation in (43), we can write

$$\begin{aligned} \Pr\{E\} &\geq \Pr\left\{ \max_{j \in [N^2/S]} \frac{|\Im((\mathbf{a}_{\mathcal{L}_o})_j^* \mathbf{v})|}{d_j} < \frac{\gamma}{\sqrt{2}} \right. \\ &\quad \left. \cap \max_{j \in [N^2/S]} \frac{|\Re((\mathbf{a}_{\mathcal{L}_o})_j^* \mathbf{v})|}{d_j} < \frac{\gamma}{\sqrt{2}} \right\} \\ &\stackrel{(a)}{\geq} \prod_{j \in [N^2/S]} \left[\Pr\left\{ \frac{|\Im((\mathbf{a}_{\mathcal{L}_o})_j^* \mathbf{v})|}{d_j} < \frac{\gamma}{\sqrt{2}} \right\} \right. \\ &\quad \left. \Pr\left\{ \frac{|\Re((\mathbf{a}_{\mathcal{L}_o})_j^* \mathbf{v})|}{d_j} < \frac{\gamma}{\sqrt{2}} \right\} \right]. \end{aligned}$$

In (a), we use Šidák's lemma [60, Theorem 1]. Now, replacing the probability values in the right-hand of the above equation with their upper limits similar to [46], we obtain (44). \square

Our proof follows a similar structure as the one in [46, Lemma 3]. We begin with the first iteration of the OMP algorithm and analyze the support recovery step. Then, by induction, we show that when the event E occurs and $\mathbf{x}_{\mathcal{L}_o}$ satisfies (34), the OMP correctly recovers the support of $\mathbf{x}_{\mathcal{L}_o}$ after K iterations where K is the sparsity level of $\mathbf{x}_{\mathcal{L}_o}$.

Now, considering the first iteration of the OMP algorithm [54] and assuming that the event E occurs, we find conditions for which the index of the selected column, i.e., the one that maximizes $|(\mathbf{a}_{\mathcal{L}_o})_j^* \mathbf{y}|/d_j$, belongs to the support Π of $\mathbf{x}_{\mathcal{L}_o}$. The correct support recovery condition in the first iteration of the OMP algorithm [54] is

$$\max_{j \in \Pi} \frac{|(\mathbf{a}_{\mathcal{L}_o})_j^* \mathbf{y}|}{d_j} > \max_{j \notin \Pi} \frac{|(\mathbf{a}_{\mathcal{L}_o})_j^* \mathbf{y}|}{d_j}. \quad (45)$$

For the right-hand side of (45), under the event E , we have

$$\begin{aligned} \max_{j \notin \Pi} \frac{|(\mathbf{a}_{\mathcal{L}_o})_j^* \mathbf{y}|}{d_j} &= \max_{j \notin \Pi} \frac{|(\mathbf{a}_{\mathcal{L}_o})_j^* \mathbf{v} + \sum_{i \in \Pi} x_{\mathcal{L}_o, i} (\mathbf{a}_{\mathcal{L}_o})_j^* (\mathbf{a}_{\mathcal{L}_o})_i|}{d_j} \\ &\stackrel{(b)}{\leq} \max_{j \notin \Pi} \frac{|(\mathbf{a}_{\mathcal{L}_o})_j^* \mathbf{v}|}{d_j} \\ &\quad + \max_{j \notin \Pi} \frac{\sum_{i \in \Pi} |x_{\mathcal{L}_o, i} (\mathbf{a}_{\mathcal{L}_o})_j^* (\mathbf{a}_{\mathcal{L}_o})_i|}{d_j} \\ &\stackrel{(c)}{<} \gamma + K \mu d_{\max} x_{\mathcal{L}_o, \max}. \end{aligned} \quad (46)$$

We use the triangular inequality in (b). In (c), we use the assumption that the event E occurs and the fact that

$$\begin{aligned} \frac{|\bar{x}_{\mathcal{L}_o, i} (\mathbf{a}_{\mathcal{L}_o})_j^* (\mathbf{a}_{\mathcal{L}_o})_i|}{d_j} &= |x_{\mathcal{L}_o, i}| \frac{|(\mathbf{a}_{\mathcal{L}_o})_j^* (\mathbf{a}_{\mathcal{L}_o})_i|}{d_j d_i} \\ &\stackrel{(d)}{\leq} d_{\max} x_{\mathcal{L}_o, \max} \mu. \end{aligned}$$

In (d), we use $\mu_o = \max_{j \neq i} \frac{|(\mathbf{a}_{\mathcal{L}_o})_j^* (\mathbf{a}_{\mathcal{L}_o})_i|}{d_j d_i}$ which is an alternative definition for the coherence of the effective CS matrix $\mathbf{A}_{\mathcal{L}_o}$

given in (30). Under the event E , for the left-hand side of (45), we have

$$\begin{aligned} &\max_{j \in \Pi} \frac{|(\mathbf{a}_{\mathcal{L}_o})_j^* \mathbf{y}|}{d_j} \\ &= \max_{j \in \Pi} \frac{|d_j^2 x_{\mathcal{L}_o, j} + (\mathbf{a}_{\mathcal{L}_o})_j^* \mathbf{v} + \sum_{i \in \Pi \setminus \{j\}} x_{\mathcal{L}_o, i} (\mathbf{a}_{\mathcal{L}_o})_j^* (\mathbf{a}_{\mathcal{L}_o})_i|}{d_j} \\ &\geq d_{\min} x_{\mathcal{L}_o, \max} \\ &\quad - \max_{j \in \Pi} \frac{|(\mathbf{a}_{\mathcal{L}_o})_j^* \mathbf{v} + \sum_{i \in \Pi \setminus \{j\}} x_{\mathcal{L}_o, i} (\mathbf{a}_{\mathcal{L}_o})_j^* (\mathbf{a}_{\mathcal{L}_o})_i|}{d_j} \\ &> d_{\min} x_{\mathcal{L}_o, \max} - \gamma - (K-1) \mu_o d_{\max} x_{\mathcal{L}_o, \max}. \end{aligned} \quad (47)$$

Note that in the first inequality, we use $\max_{j \in \Pi} |d_j x_{\mathcal{L}_o, j}| \geq d_{\min} x_{\mathcal{L}_o, \max}$. Hence, from (46) and (47) we can write

$$\begin{aligned} \max_{j \in \Pi} \frac{|(\mathbf{a}_{\mathcal{L}_o})_j^* \mathbf{y}|}{d_j} &> d_{\min} x_{\mathcal{L}_o, \max} - (2K-1) \mu_o d_{\max} x_{\mathcal{L}_o, \max} \\ &\quad - 2\gamma + \max_{j \notin \Pi} \frac{|(\mathbf{a}_{\mathcal{L}_o})_j^* \mathbf{y}|}{d_j}. \end{aligned} \quad (48)$$

From (48), we observe that under the event E , when

$$d_{\min} x_{\mathcal{L}_o, \max} - (2K-1) \mu_o d_{\max} x_{\mathcal{L}_o, \max} \geq 2\gamma, \quad (49)$$

equation (45) holds and therefore the selected entry in the first iteration of the OMP algorithm [54] will belong to the support of $\mathbf{x}_{\mathcal{L}_o}$. We note that (34) implies (49). Next, by using an induction-based technique as in [46, Theorem 4], we can show that under (34) and the event E , the OMP algorithm will successfully recover the entire support Π of $\mathbf{x}_{\mathcal{L}_o}$ after K iterations. Finally, by following our approach in Theorem 2 of [2], we can derive the upper-bound (36) for the MSE in $\hat{\mathbf{x}}_{\mathcal{L}_o}$.

REFERENCES

- [1] H. Masoumi, N. J. Myers, G. Leus, S. Wahls, and M. Verhaegen, "Structured sensing matrix design for in-sector compressed mmWave channel estimation," in *Proc. IEEE 23rd Int. Workshop Signal Process. Adv. Wireless Comm. (SPAWC)*, Jul. 2022, pp. 1–5.
- [2] H. Masoumi, M. Verhaegen, and N. J. Myers, "Analysis of orthogonal matching pursuit for compressed sensing in practical settings," in *Proc. IEEE Stat. Signal Process. Workshop (SSP)*, Jul. 2023, pp. 170–174.
- [3] T. S. Rappaport et al., "Wireless communications and applications above 100 GHz: Opportunities and challenges for 6G and beyond," *IEEE Access*, vol. 7, pp. 78729–78757, 2019.
- [4] H. Sarrideen, M.-S. Alouini, and T. Y. Al-Naffouri, "An overview of signal processing techniques for terahertz communications," *Proc. IEEE*, vol. 109, no. 10, pp. 1628–1665, Oct. 2021.
- [5] I. P. Roberts, J. G. Andrews, H. B. Jain, and S. Vishwanath, "Millimeter-wave full duplex radios: New challenges and techniques," *IEEE Wireless Commun.*, vol. 28, no. 1, pp. 36–43, Feb. 2021.
- [6] Z. Xiao, T. He, P. Xia, and X. Xia, "Hierarchical codebook design for beamforming training in millimeter-wave communication," *IEEE Trans. Wireless Commun.*, vol. 15, no. 5, pp. 3380–3392, May 2016.
- [7] J. Brady, N. Behdad, and A. M. Sayeed, "Beamspace MIMO for millimeter-wave communications: System architecture, modeling, analysis, and measurements," *IEEE Trans. Antennas Propag.*, vol. 61, no. 7, pp. 3814–3827, Jul. 2013.
- [8] S. Noh, M. D. Zoltowski, and D. J. Love, "Multi-resolution codebook and adaptive beamforming sequence design for millimeter wave beam alignment," *IEEE Trans. Wireless Commun.*, vol. 16, no. 9, pp. 5689–5701, Sep. 2017.
- [9] Z. Xiao, H. Dong, L. Bai, P. Xia, and X.-G. Xia, "Enhanced channel estimation and codebook design for millimeter-wave communication," *IEEE Trans. Veh. Technol.*, vol. 67, no. 10, pp. 9393–9405, Oct. 2018.

- [10] P. Raviteja, Y. Hong, and E. Viterbo, "Analog beamforming with low resolution phase shifters," *IEEE Wireless Commun. Lett.*, vol. 6, no. 4, pp. 502–505, Aug. 2017.
- [11] C.-R. Tsai and A.-Y. Wu, "Structured random compressed channel sensing for millimeter-wave large-scale antenna systems," *IEEE Trans. Signal Process.*, vol. 66, no. 19, pp. 5096–5110, Oct. 2018.
- [12] P. A. Eliasi, S. Rangan, and T. S. Rappaport, "Low-rank spatial channel estimation for millimeter wave cellular systems," *IEEE Trans. Wireless Commun.*, vol. 16, no. 5, pp. 2748–2759, May 2017.
- [13] A. Alkhateeb, G. Leus, and R. W. Heath, "Compressed sensing based multi-user millimeter wave systems: How many measurements are needed?" in *Proc. IEEE Int. Conf. Acoust., Speech Signal Process. (ICASSP)*, Apr. 2015, pp. 2909–2913.
- [14] N. J. Myers, A. Mezghani, and R. W. Heath, "FALP: Fast beam alignment in mmWave systems with low-resolution phase shifters," *IEEE Trans. Commun.*, vol. 67, no. 12, pp. 8739–8753, Dec. 2019.
- [15] Z. Marzi, D. Ramasamy, and U. Madhoo, "Compressive channel estimation and tracking for large arrays in mm-wave picocells," *IEEE J. Sel. Topics Signal Process.*, vol. 10, no. 3, pp. 514–527, Apr. 2016.
- [16] E. Vlachos, G. C. Alexandropoulos, and J. Thompson, "Massive MIMO channel estimation for millimeter wave systems via matrix completion," *IEEE Signal Process. Lett.*, vol. 25, no. 11, pp. 1675–1679, Nov. 2018.
- [17] W. Ma, C. Qi, Z. Zhang, and J. Cheng, "Sparse channel estimation and hybrid precoding using deep learning for millimeter wave massive MIMO," *IEEE Trans. Commun.*, vol. 68, no. 5, pp. 2838–2849, May 2020.
- [18] W. Wang and W. Zhang, "Jittering effects analysis and beam training design for UAV millimeter wave communications," *IEEE Trans. Wireless Commun.*, vol. 21, no. 5, pp. 3131–3146, May 2022.
- [19] A. Ali, N. González-Prelcic, and R. W. Heath, "Millimeter wave beam-selection using out-of-band spatial information," *IEEE Trans. Wireless Commun.*, vol. 17, no. 2, pp. 1038–1052, Feb. 2018.
- [20] P.-C. Chen and P. P. Vaidyanathan, "Convolutional beamspace for linear arrays," *IEEE Trans. Signal Process.*, vol. 68, pp. 5395–5410, 2020.
- [21] P.-C. Chen and P. P. Vaidyanathan, "Hybrid convolutional beamspace for DOA estimation of millimeter wave sources," in *Proc. 56th Asilomar Conf. Signals, Syst., Comput.*, Oct. 2022, pp. 86–90.
- [22] S. Chiu, N. Ronquillo, and T. Javidi, "Active learning and CSI acquisition for mmWave initial alignment," *IEEE J. Sel. Areas Commun.*, vol. 37, no. 11, pp. 2474–2489, Nov. 2019.
- [23] S.-E. Chiu and T. Javidi, "Low complexity sequential search with size-dependent measurement noise," *IEEE Trans. Inf. Theory*, vol. 67, no. 9, pp. 5731–5748, Sep. 2021.
- [24] X. Song, S. Haghighatshoar, and G. Caire, "A scalable and statistically robust beam alignment technique for millimeter-wave systems," *IEEE Trans. Wireless Commun.*, vol. 17, no. 7, pp. 4792–4805, Jul. 2018.
- [25] E. Khordad, I. B. Collings, S. V. Hanly, and G. Caire, "Compressive sensing-based beam alignment schemes for time-varying millimeter-wave channels," *IEEE Trans. Wireless Commun.*, vol. 22, no. 3, pp. 1604–1617, Mar. 2023.
- [26] N. J. Myers, A. Mezghani, and R. W. Heath Jr., "Spatial zadoff-chu modulation for rapid beam alignment in mmWave phased arrays," in *Proc. IEEE Globecom Workshops (GC Wkshps)*, Dec. 2018, pp. 1–6.
- [27] F. Kraemer and H. Rauhut, "Structured random measurements in signal processing," *GAMM-Mitteilungen*, vol. 37, no. 2, pp. 217–238, Nov. 2014.
- [28] D. Steinmetzer, D. Wegemer, M. Schulz, J. Widmer, and M. Hollick, "Compressive millimeter-wave sector selection in off-the-shelf IEEE 802.11ad devices," in *Proc. 13th Int. Conf. Emerg. Netw. Exp. Technol.*, 2017, pp. 414–425.
- [29] V. Raghavan et al., "Millimeter-wave MIMO prototype: Measurements and experimental results," *IEEE Commun. Mag.*, vol. 56, no. 1, pp. 202–209, Jan. 2018.
- [30] A. Alhamed, G. Gültepe, and G. M. Rebeiz, "64-element 16–52-GHz transmit and receive phased arrays for multiband 5G-NR FR2 operation," *IEEE Trans. Microw. Theory Techn.*, vol. 71, no. 1, pp. 360–372, Jan. 2023.
- [31] S. Zahir, O. D. Gurbuz, A. Kar-Roy, S. Raman, and G. M. Rebeiz, "60-GHz 64- and 256-elements wafer-scale phased-array transmitters using full-reticle and subreticle stitching techniques," *IEEE Trans. Microw. Theory Techn.*, vol. 64, no. 12, pp. 4701–4719, Dec. 2016.
- [32] D. Tse and P. Viswanath, *Fundamentals of Wireless Communication*. Cambridge, U.K.: Cambridge Univ. Press, 2005.
- [33] S. Sun, G. R. MacCartney, and T. S. Rappaport, "A novel millimeter-wave channel simulator and applications for 5G wireless communications," in *Proc. IEEE Int. Conf. Commun. (ICC)*, May 2017, pp. 1–7.
- [34] T. Nitsche, C. Cordeiro, A. B. Flores, E. W. Knightly, E. Perahia, and J. C. Widmer, "IEEE 802.11 ad: Directional 60 GHz communication for multi-gigabit-per-second Wi-Fi," *IEEE Commun. Mag.*, vol. 52, no. 12, pp. 132–141, Dec. 2014.
- [35] P. F. M. Smulders, "Statistical characterization of 60-GHz indoor radio channels," *IEEE Trans. Antennas Propag.*, vol. 57, no. 10, pp. 2820–2829, Oct. 2009.
- [36] O. Kome, L. Cen, L. Hanqing, and Y. Rui, "Further details on multi-stage, multi-resolution beamforming training in 802.11 ay, doc," InterDigit., San Diego, CA, USA, Tech. Rep. 01, 2016.
- [37] *IEEE Standard for Information Technology–Telecommunications and Information Exchange Between Systems—Local and Metropolitan Area Networks—Specific Requirements—Part 11: Wireless LAN Medium Access Control (MAC) and Physical Layer (PHY) Specifications*, IEEE Standard 802.11-2020, 2021, pp. 1–4379.
- [38] M. Giordani, M. Mezzavilla, and M. Zorzi, "Initial access in 5G mmWave cellular networks," *IEEE Commun. Mag.*, vol. 54, no. 11, pp. 40–47, Nov. 2016.
- [39] A. K. Jain, *Fundamentals of Digital Image Processing*. Upper Saddle River, NJ, USA: Prentice-Hall, 1989.
- [40] D. G. Manolakis and V. K. Ingle, *Applied Digital Signal Processing: Theory and Practice*. Cambridge, U.K.: Cambridge Univ. Press, 2011.
- [41] A. C. Kak and M. Slaney, *Principles of Computerized Tomographic Imaging*. Philadelphia, PA, USA: SIAM, 2001.
- [42] P. Stoica, H. He, and J. Li, "On designing sequences with impulse-like periodic correlation," *IEEE Signal Process. Lett.*, vol. 16, no. 8, pp. 703–706, Aug. 2009.
- [43] K. Li, L. Gan, and C. Ling, "Convolutional compressed sensing using deterministic sequences," *IEEE Trans. Signal Process.*, vol. 61, no. 3, pp. 740–752, Feb. 2013.
- [44] E. Candès and J. Romberg, "Sparsity and incoherence in compressive sampling," *Inverse Problems*, vol. 23, no. 3, p. 969, Apr. 2007.
- [45] M. Lustig, D. Donoho, and J. M. Pauly, "Sparse MRI: The application of compressed sensing for rapid MR imaging," *Magn. Reson. Med.*, vol. 58, no. 6, pp. 1182–1195, 2007.
- [46] Z. Ben-Haim, Y. C. Eldar, and M. Elad, "Coherence-based performance guarantees for estimating a sparse vector under random noise," *IEEE Trans. Signal Process.*, vol. 58, no. 10, pp. 5030–5043, Oct. 2010.
- [47] M. Golay, "Complementary series," *IRE Trans. Inf. Theory*, vol. 7, no. 2, pp. 82–87, Apr. 1961.
- [48] K. V. Mishra and Y. C. Eldar, "Sub-nyquist channel estimation over IEEE 802.11ad link," in *Proc. Int. Conf. Sampling Theory Appl. (SampTA)*, Jul. 2017, pp. 355–359.
- [49] L. Zhao, J. Song, P. Babu, and D. P. Palomar, "A unified framework for low autocorrelation sequence design via majorization–minimization," *IEEE Trans. Signal Process.*, vol. 65, no. 2, pp. 438–453, Jan. 2017.
- [50] J. Jedwab, C. Mitchell, F. Piper, and P. Wild, "Perfect binary arrays and difference sets," *Discrete Math.*, vol. 125, nos. 1–3, pp. 241–254, Feb. 1994.
- [51] R. Frank, S. Zadoff, and R. Heimiller, "Phase shift pulse codes with good periodic correlation properties (Corresp.)," *IEEE Trans. Inf. Theory*, vol. IT-8, no. 6, pp. 381–382, Oct. 1962.
- [52] D. C. Chu, "Polyphase codes with good periodic correlation properties," *IEEE Trans. Inf. Theory*, vol. IT-18, no. 4, pp. 531–532, Jul. 1972.
- [53] N. Zhang and S. W. Golomb, "Polyphase sequence with low autocorrelations," *IEEE Trans. Inf. Theory*, vol. 39, no. 3, pp. 1085–1089, May 1993.
- [54] M. Gharavi-Alkhansari and T. S. Huang, "A fast orthogonal matching pursuit algorithm," in *Proc. IEEE Int. Conf. Acoust., Speech Signal Process. (ICASSP)*, May 1998, pp. 1389–1392.
- [55] W. Dai and O. Milenkovic, "Subspace pursuit for compressive sensing signal reconstruction," *IEEE Trans. Inf. Theory*, vol. 55, no. 5, pp. 2230–2249, May 2009.
- [56] S. Boyd and J. Park, "Subgradient methods," Lect. Notes EE364b, Stanford Univ., Stanford, CA, USA, Tech. Rep. 01, 2014.
- [57] S. Boyd, S. P. Boyd, and L. Vandenberghe, *Convex Optimization*. Cambridge, U.K.: Cambridge Univ. Press, 2004.
- [58] Y. Ghasempour, C. R. C. M. da Silva, C. Cordeiro, and E. W. Knightly, "IEEE 802.11ay: Next-generation 60 GHz communication for 100 Gb/s Wi-Fi," *IEEE Commun. Mag.*, vol. 55, no. 12, pp. 186–192, Dec. 2017.

- [59] J. Ziniel and P. Schniter, "Dynamic compressive sensing of time-varying signals via approximate message passing," *IEEE Trans. Signal Process.*, vol. 61, no. 21, pp. 5270–5284, Nov. 2013.
- [60] Z. Šidák, "Rectangular confidence regions for the means of multivariate normal distributions," *J. Amer. Stat. Assoc.*, vol. 62, no. 318, pp. 626–633, 1967.



Hamed Masoumi (Graduate Student Member, IEEE) received the B.Sc. and M.Sc. degrees in electrical engineering from the Amirkabir University of Technology (AUT), Tehran, Iran, in 2016 and 2019, respectively. He is currently pursuing the Ph.D. degree with Delft Center for Systems and Control (DCSC), Delft University of Technology (TU Delft), The Netherlands. His research interests include the intersection of wireless communications and signal processing. He was a recipient of the Best Student Paper Award at the IEEE SPAWC 2022.



Michel Verhaegen (Member, IEEE) received the Engineering degree in aeronautics from Delft University of Technology, Delft, The Netherlands, in 1982, and the Ph.D. degree in applied sciences from the Catholic University of Leuven, Belgium, in 1985. During his graduate study, he held a research assistantship sponsored by the Flemish Institute for Scientific Research (IWT). From 1985 to 1994, he was a Research Fellow of the U.S. National Research Council (NRC), affiliated with the NASA Ames Research Center, CA, USA; and of the Dutch Academy of Arts and Sciences, affiliated with the Network Theory Group, Delft University of Technology. From 1994 to 1999, he was an Associate Professor with the Control Laboratory, Delft University of Technology. He was a Full Professor with the Faculty of Applied Physics,

University of Twente, The Netherlands, in 1999. In 2001, he moved back to Delft University of Technology, where he is currently a member of Delft Center for Systems and Control. He has held short sabbatical leaves at the University of Uppsala, McGill, Lund; and German Aerospace Research Center (DLR), Munich, and is participating in several European Research Networks. His research interests include the interdisciplinary domain of numerical algebra and system theory. In this field, he has published over 150 peer-reviewed articles in top journals in the field of systems and control and optical systems. This includes 38 articles in IEEE TRANSACTIONS and 17 articles in *Automatica* journal. Currently, he has a renewed interest in broadening the field of system identification in areas, such as imaging systems, data-driven fault detection, and control. He received the Prestigious International Federation for Automatic Control (IFAC) Fellow Award in 2014. This award is given to persons who have made outstanding and extraordinary contributions in the field of interest of IFAC, in the role of an Engineer/Scientist, a Technical Leader, or an Educator. He was a recipient of the Advanced Personal Grant from European Research Council in 2017.



Nitin Jonathan Myers (Member, IEEE) received the joint B.Tech. and M.Tech. degree in electrical engineering from Indian Institute of Technology (IIT) Madras in 2016 and the Ph.D. degree in electrical and computer engineering (ECE) from The University of Texas at Austin (UT Austin) in 2020.

He is currently a tenured Assistant Professor with Delft Center for Systems and Control, Delft University of Technology (TU Delft). Prior to joining TU Delft, he was a Senior Engineer with the 5G Modem Research and Development Team, Samsung Semiconductor Inc., San Diego. His research interests include optimization and multi-dimensional signal processing, with applications to communications and sensing.

Dr. Myers received the DAAD WISE Scholarship in 2014 and a Silver Medal, Institute Merit Prize, in 2016, during his undergraduate days at IIT Madras. At UT Austin, he received the University Graduate Continuing Fellowship 2019–2020 and the 2018 and 2019 ECE Research Awards from the Cockrell School of Engineering. He was recognized as an Exemplary Reviewer by IEEE TRANSACTIONS ON COMMUNICATIONS in 2019 and IEEE WIRELESS COMMUNICATIONS LETTERS in 2018. His research won the IEEE ICASSP 2020 Video Contest Runner-Up and the Best Student Paper Award at IEEE SPAWC 2022. He was recognized by TU Delft as the Best Lecturer in the second year of the bachelor's program in mechanical engineering (2021–2022).